2005

Process Development and Characterization of Sol-Gel Lead Zirconate Titanate Films for Fabrication of Flexural Plate Wave Devices

Praveen Kumar Sekhar
University of South Florida

Scholar Commons Citation

Sekhar, Praveen Kumar, "Process Development and Characterization of Sol-Gel Lead Zirconate Titanate Films for Fabrication of Flexural Plate Wave Devices" (2005). *USF Tampa Graduate Theses and Dissertations.*
https://digitalcommons.usf.edu/etd/2960

Process Development and Characterization of Sol-Gel Lead Zirconate Titanate Films for Fabrication of Flexural Plate Wave Devices

by

Praveen Kumar Sekhar

A thesis submitted in partial fulfillment
of the requirement for the degree of
Master of Science in Electrical Engineering
Department of Electrical Engineering
College of Engineering
University of South Florida

Major Professor: Shekhar Bhansali, Ph.D.
Elias K. Stefanakos, Ph.D.
Larry Langebrake, P.E.

Date of Approval:
March 29, 2005

Keywords: Annealing, PZT, Pyrolysis, Ultra-thin membrane, Acoustic Waves

Acknowledgements

I sincerely express my gratitude to Dr.Shekhar Bhansali for his whole-hearted support, tremendous faith and invaluable suggestions towards my research. I would like to thank Dr.Stefanakos and Larry Langebrake for serving as my committee members. Special thanks to largo team for their excellent processing capabilities especially Dr. John Bumgarner, Dr. Shinzo Onishi, Dave and Sean. From the Tampa team, Dr. Senthil Sambandam, Subbu, Shyam, Kevin, Saravana, Sriram and other colleagues for their support. Robert Tufts, Rich Everly and Jay Bieber for their excellent co-operation and maintenance of equipments in the NNRC user facility. Last but not the least I am greatly indebted to my family members for all their love and sacrifice that made this possible.

Table of Contents

List of Tables

List of Figures

Process Development and Characterization of Sol-Gel Lead Zirconate Titanate Films for Fabrication of Flexural Plate Wave Devices

Praveen Kumar Sekhar

ABSTRACT

In recent years, research on development of chemical, biological and hazardous gas sensors for homeland security have attracted great deal of interest. Actuators possessing high sensitivity, easy fabrication techniques and excellent integration compatibility are in great demand. Towards this need, the development and characterization of improved sol-gel processing for in-house fabrication of highly sensitive and reliable Flexural Plate Wave (FPW) device was pursued

This work focuses on an experimental design approach to improve texture and morphology of PZT thin film by systematically controlling the spin, pyrolysis and anneal cycles. The process alterations resulted in an 8-fold increase in the relative intensity of perovskite (111) phase, which consequently yielded a two fold improvement in remnant polarization and coercive field compared to industry recommended processes. Optimized films showed a remnant polarization of 95.7μC/cm^2 and coercive filed of 56.7 KV/cm respectively. Several designs of the interdigitated electrodes (IDE/IDT) with varying periodicity are investigated to characterize the output response of the device. The FPW device is fabricated using 2μm thick silicon nitride membrane on Pt bottom electrode with Ti/TiN as the adhesion layer. A highly sensitive flexural plate wave sensor based on the revised PZT recipe is successfully fabricated.

Chapter 1
Introduction

1.1 Objective

The main objective of this thesis is to develop an optimized process for the enhancement of the texture and improvement of the ferroelectric properties of sol-gel derived Lead Zirconate Titanate (PZT) thin films. The improvement in the ferroelectric properties in turn will improve the sensitivity and stability of a flexural plate wave (FPW) device that is being built. The FPW device is a type of acoustic device that can be used both as a sensor and an actuator. Basic properties and classification of acoustic devices is discussed here under.

1.2 Classification of Acoustic Devices

Acoustic devices are gaining enormous interest in chemical and biological sensing due to the inherent sensitivity, resolution, reliability and relative ease in fabrication. They are classified as (a) Quartz Crystal Microbalances (QCMs), (b) Surface Acoustic Wave (SAW) device, (c) Acoustic Plate Mode (APM) device, and (d) Flexural Plate Wave (FPW) device. The above listed devices work on different modes of generation and propagation of acoustic waves. In order to get a better understanding about the functioning of the devices, it is necessary to understand the generation mode of the waves. Figure 1.1 shows a schematic sketch of different types of acoustic devices [1].

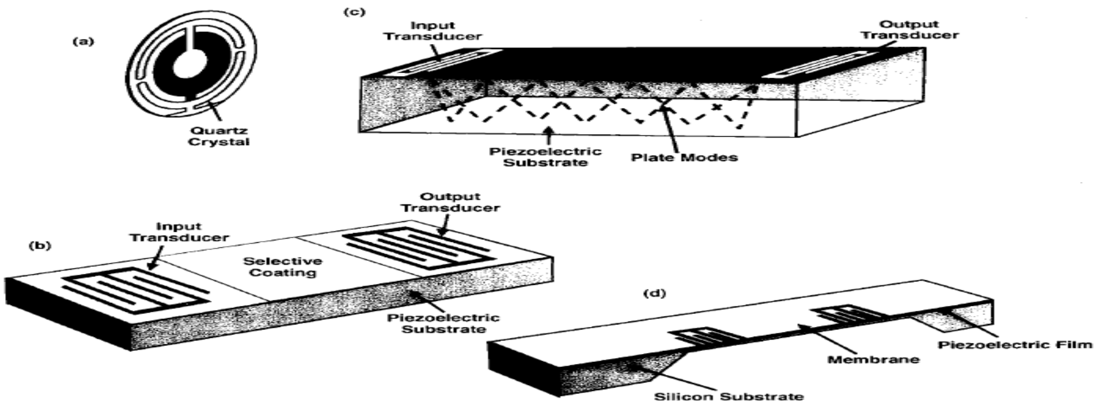

Figure 1.1 Types of Acoustic Devices (a) Quartz Crystal Microbalances (QCMs), (b) Surface Acoustic Delay Line(SAW), (c) Acoustic Plate Mode(APM), (d) Flexural Plate Wave Delay Line Acoustic Devices

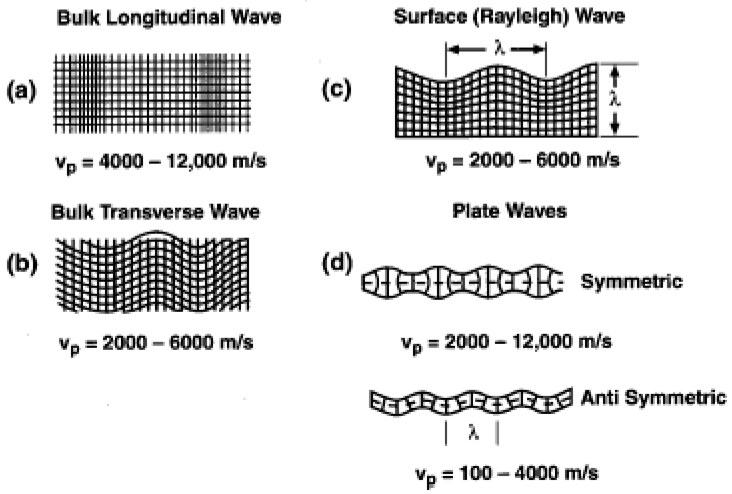

Figure 1.2 Principle of Wave Propagation (a) Bulk Longitudinal Wave in Unbounded Solid, (b) Bulk Transverse Wave, (c) Rayleigh Wave, (d) Plate Waves [1]

Figure 1.2 represents the principle of wave propagation on different acoustic devices. Essentially, elastic deformation of solid particles with various boundary conditions constitutes different acoustic waves and hence different classes of sensor/actuator systems. As seen in Figure 1.2, when the particle displacement is parallel to the direction of propagation in the unbounded state, it is referred to as bulk longitudinal wave, and when the particle displacement is perpendicular, it is referred to as bulk transverse wave. Waves with elliptical displacement of particles constrained by a single plane boundary are termed as Rayleigh (surface) waves. Adding a second boundary plane in the path of the former generates Lamb (flexural) waves.

1.3 Relevance of Acoustic Sensing

The wave parameters like frequency, amplitude and phase in an acoustic device are very sensitive to the immediate environment. Unlike many other sensing mechanisms, the acoustic devices are known for their sensitivity due to surface phenomenon. Hence, the active sensing surface is generally placed between two transducers resulting in low loss of acoustic signals. An incremental variation on the surface, due to the interaction of the sensing element with the environment, has pronounced effect on the wave parameters. Since the wave disturbance can be directly correlated to the change in chemical and physical properties of analytes, acoustic sensing becomes a more reliable scheme of detection.

1.4 Significance of Flexural Plate Waves

A flexural plate wave device when compared to other types of acoustic devices possesses higher sensitivity. This is discussed in detail in the forthcoming chapters. In a FPW device, the entire acoustic energy is confined within an ultra-thin membrane. A small perturbation on the surface results in significant change in wave properties. Additionally, in a FPW device, the actuating electrodes can be isolated from the medium under investigation. This is an added benefit in fluidic applications where the device overcomes shorting and packaging challenges while allowing the analyte of interest to be preserved for further use. These devices find application in microfluidics due to their low phase velocity profile and high energy concentration. The transparent nature of PZT membrane allows efficient optical validation of targets, if immobilized on the surface.

1.5 Piezoelectric Medium

Acoustic sensors requires piezoelectric medium for generation of waves. The wave emanation can be explained in terms of crystal re-ordering. In a piezoelectric crystal, at equilibrium, inherent crystal strain is balanced by the internal polarization force. When disturbed either by applying external electric field or stress, de-polarization waves are emitted, acting as a restoring force to maintain equilibrium. The magnitude of the force emitted is directly proportional to stress applied, crystal orientation and arrangement of ferroelectric domains, both functions of crystal morphology. Hence a good actuation force (proportional to electromechanical coupling) would depend on the texture and morphology of the piezoelectric material. An ideal piezoelectric should have following properties: 1) high value of electromechanical coupling, 2) good adhesion to substrate, 3) chemical Inertness, 4) resistance to environmental variations, 5) VLSI processing compatibility and 6) cost-effectiveness. Even though numerous materials exhibit piezoelectricity, there are certain materials that have high electromechanical coupling coefficients and hence provide higher actuation force. ZnO, AlN and PZT have high electromechanical coupling coefficients and hence provide higher actuation force.

Table 1.1 Comparison of Electromechanical Coupling Coeffients for Different Piezoelectric Materials [2]

Coefficients	ZnO	AlN	PVDF	PZT
k_{31}(%)	7.4	6.5	0.18	7 to 15

Table 1.1 [2] shows the comparative study on the electromechanical coupling factor of three materials. The electromechanical coupling factor (k_{31}) is defined as the ratio of mechanical energy accumulated in response to an electrical input. From the above table it can be inferred that PZT has the highest coupling coefficient value indicating the higher levels of sensitivity. There are various methods of depositing PZT which would be discussed in chapter 4. In this work, sol-gel based PZT is used as the piezoelectric material. The reason for using the specific deposition process will be explained in forthcoming chapters. The sol-gel parameters are optimized to achieve higher actuation force. As the concept evolves, it is necessary to cite its potential applications in real world. Hence application in the sensing domain is chosen.

1.6 Applications

Flexural plate wave sensors have widespread applications as chem./bio sensors [3], ultrasonic pumps [4], gas sensors [5] and in various metrology instrumentations [6]. Table 1.2 lists out the expanded view of the above mentioned applications.

Table 1.2 Flexural Plate Wave Sensor Applications

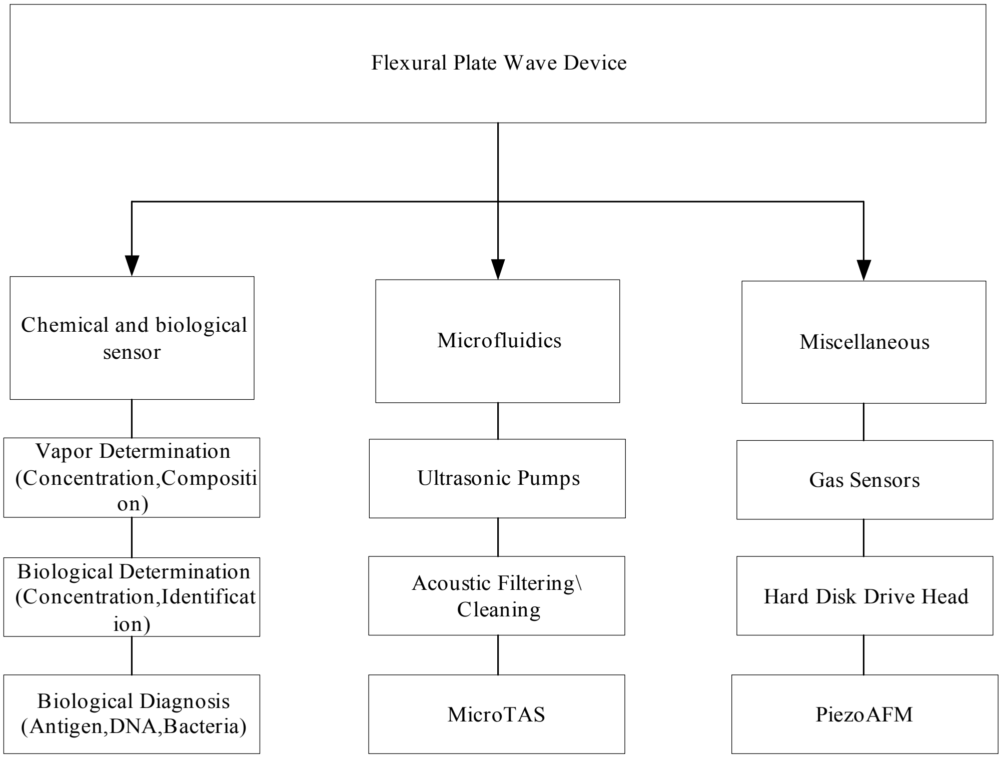

1.7 Future Application

One of the most promising future applications of a FPW resonator is in the field of wireless communication and sensing leading to on-chip communication modules. Due to high selectivity to noise, inertness to the surrounding environment and high sensitivity, it would outperform SAW devices.

1.8 Salient Features of this Research

1. The use of PZT (lead zirconium titanate) as the piezoelectric material which has high electromechanical coupling coefficient.

2. In-house optimization of sol-gel processing conditions to enhance the texture and morphology of PZT.

1.9 Organization of the Thesis

Chapter 2- Discusses the theory behind piezoelectric actuation, generation of acoustic waves and types of acoustic devices. The advantage and disadvantage of each device is highlighted with an explanation of the superiority of FPW over other devices.

Chapter 3-Focuses on the different piezoelectric materials used to fabricate flexural plate wave devices. The rationale for the choice of PZT as a piezoelectric material is presented. Various methods of depositing PZT are studied with an emphasize on sol-gel based technique.

Chapter 4-Deals with the processing conditions and requirements of sol-gel PZT. A literature review on earlier sol-gel work is presented and past results are analyzed. The process variations for an improved texture and morphology are discussed and illustrated

Chapter 5-Concentrates on the fabrication of a flexural plate wave device, focusing on issues, challenges and their solution as progress is made towards the implementation of the final structure.

Chapter 6-Discusses the results after optimization and a brief note on future work is presented

Chapter 2

Piezoelectricity and Acoustics

This chapter focuses on the basic concept of piezoelectricity. After explaining the concept of piezoelectricity, different types of acoustic sensors are discussed with emphasis on understanding the flexural plate wave based actuation methodology and its advantages over other acoustic devices.

2.1 Definition of Piezoelectricity

Piezoelectricity is a phenomenon exhibited by non-centrosymmetric crystals where in the stress applied to the material results in the development of electric polarization or surface charges. Hence, tensile and compressive stresses [8] generate voltages of opposite polarity and, the magnitude of the voltage generated is proportional to the force applied. Conversely an applied electric field induces a strain proportional to the magnitude of applied electric field. The former is referred to as the direct effect and used in sensing while the latter is referred to as converse effect used in actuation mechanisms. Figure 2.1 is the schematic illustration of this effect. As can be seen, application of a force ‘F’ induces incremental charge ΔQ detected by a voltmeter. Conversely when the material is subjected to a potential ‘V’, the surface is strained, which is detected by position gauges.

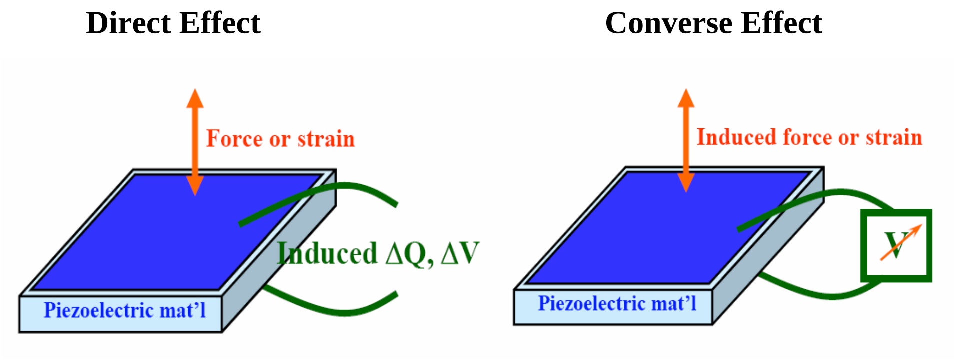

Figure 2.1 Pictorial Depicting Piezoelectricity [8]

Where,

ΔQ, ΔV = Incremental surface charge and induced potential due to applied mechanical strain respectively.

The accrued piezoelectric effect from a non-centrosymmetric crystal structure is enhanced by the orienting all the domains in a particular order. This is accomplished through a process of poling. Poling the material improves the piezoelectric properties which in turn yields higher actuation force, as explained below.

2.2 Direct Piezoelectric Effect

1. Applied stress on piezoelectric materials induces electric polarization. The direct effect is governed by three fundamental equations:-

$$P = d\sigma \ (\mathrm{C/m^2}) \ \ldots \ (1)$$

Where,

P=Electric Polarization

d=Piezoelectric constant (C/N)

σ =Applied Stress (N/m^2)

2. The polarization P is linked to the electric displacement D(C/m^2) and electric field E (KV/cm) by

$$D = \varepsilon_0 E + P \ \ldots \ (2)$$

3) The electric field and polarization are related by

$$P = \varepsilon_0 E \chi \ldots (3)$$

Where,

χ = Electric Susceptibility

2.3 Poling

In piezoelectric materials, spontaneous polarization is generated from non-centrosymmetric arrangement of atoms in a unit cell. The adjoining dipoles of these unit cells form regions of local alignment referred to as domains. Alignment of all domains gives a net dipole moment and polarization. Generally, in a poly-crystalline material the direction of polarization among domains is random in nature and this which accounts for low piezoelectric properties in potential applications. In these materials the domains are aligned by subjecting the crystal to a strong electric field (around 10E-5 V\m) usually at a temperature below the Curie temperature. When the electric field is removed, the crystal remains permanently poled. This process is called poling. Figure 2.2 illustrates the poling phenomenon. [9]

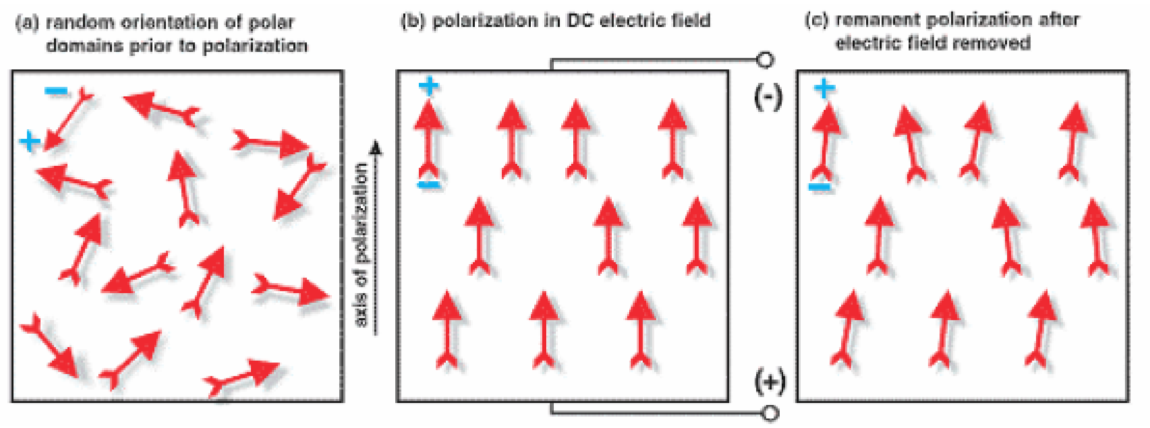

Figure 2.2 Schematic of the Orientation During Poling [9]

2.4 Hysteresis Curve

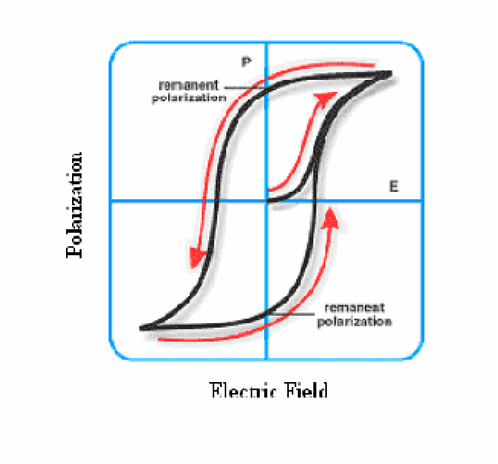

Figure 2.3 Typical Hysteresis Curve [9]

Figure 2.3 illustrates a typical hysteresis curve for piezoelectric materials with polarization on Y-axis and electric field on X-axis. When an unpolarized sample of ferroelectric material is subjected to increasing electric field, the dipoles become increasingly aligned with the field. This phenomenon is traced as the initial linear rise which stops at a particular value of electric field. The material is then said to have reached saturation polarization (P_s). The dipoles are all aligned with the field. If the field is now reduced to zero, they do not return to their original alignment (i.e. the alignment before the field was applied) since there are several preferred directions within the crystallites and the dipoles remain in the ones most closely aligned with the original field. The polarization does not fall back to zero but to a value somewhat lower than the saturation polarization known as the remnant polarization (Pr). If the field is now increased in the opposite direction, the polarization of the sample initially falls to zero and then increases in the negative direction until it reaches a saturation polarization –*Ps*. If the field is again reduced to zero, the polarization falls to the remnant polarization -*Pr* and finally, if the field is increased in the positive direction again, the polarization will fall to zero and then eventually return to Ps. The ferroelectric properties are of the material directly affecting the actuator performance. It is necessary to understand the different types of acoustic devices as the concept of piezoelectricity is understood.

2.5 Acoustic Devices

Acoustic devices are versatile devices popular in chemical and biological sensing. As stated earlier, these devices are based on the disturbance induced in the path of wave propagation (similar to waves generated in ocean). A fundamental understanding of wave generation in different acoustic devices is presented next.

2.6 Quartz Crystal Microbalances (QCMs)

QCM belongs to the family of longitudinal wave devices. It is made up of a piezoelectric crystal covered with metal film acting as electrodes. Figure 2.4 illustrates an AT-Cut Quartz disc.

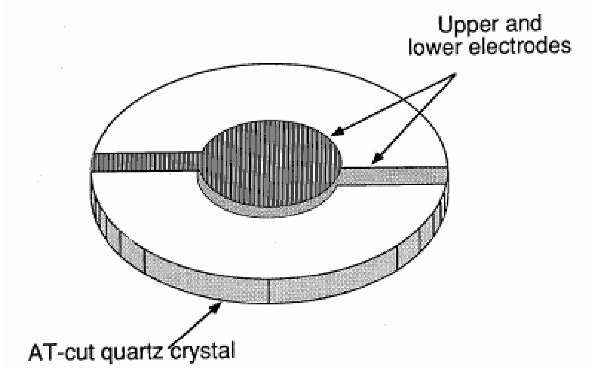

Figure 2.4 Schematic of a QCM [1]

In QCMs, system frequency is a function of thickness of the quartz plate and its electrodes, with the thickness being inversely proportional to the sensitivity and operating frequency. In this device, the application of voltage between the electrodes results in shear deformation. The device can be excited in a number of resonant shear modes with maximum displacement on crystal faces. Surface loading perturbs the wave generated thus acting as a sensor. Some of the disadvantages are handling ultra-thin fragile structures, monolithic integration, and high sensitivity to temperature.

2.7 Acoustic Plate Mode (Shear Horizontal Acoustic Plate Mode (SH-APM))

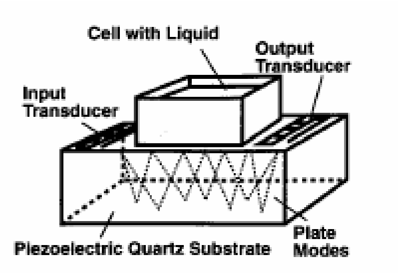

Figure 2.5 Schematic of SH-APM [1]

Figure 2.5 represents a shear horizontal acoustic plate mode device. Devices that have particle displacements parallel to the surface of the device and normal to the direction of propagation come under the category of plate mode devices. They consist of thin single-crystal quartz plates which serve as waveguides transferring energy between the upper and lower plates. They are mainly used for sensing liquids. Absence of the vertical component of the wave limits the excessive coupling of the acoustic energy to the environment leading to the propagation of waves in liquids unlike SAW where the wave is attenuated in a dissipative medium. The structure of these devices is similar to that of a SAW. The advantages of APM devices are high frequency operation, suitability for integrated chem/bio sensors and simple packaging scheme. However, the sensitivity of the device is reduced due to the mode interference.

2.8 Surface Acoustic Wave (SAW)

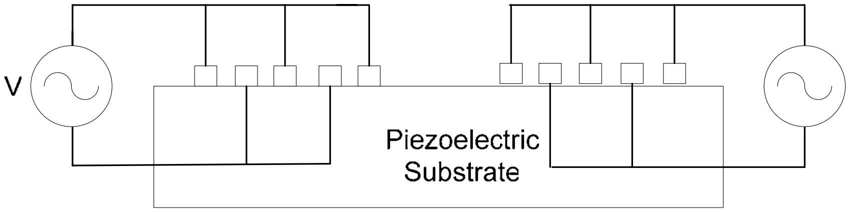

Figure 2.6 Cross Section of the SAW Device

Figure 2.6 schematically sketches the cross-section of a SAW device. In a SAW, the substrate is piezoelectric in nature. Due to the stress free boundary imposed by the piezoelectric substrate, the acoustic energy carried by the wave is totally confined to the surface making it extremely sensitive to surface perturbations. Unlike QCMs, waves are simultaneously generated and detected by lithographically patterned interdigital electrodes (IDEs or IDTs). When an alternating voltage is applied between periodic IDTs, a strain field is produced translating into a standing wave. For efficient transduction of energy, the periodicity of the IDTs is made equal to the acoustic wavelength. The advantages of SAW devices are the ease in fabrication, high frequency operation and simple packaging scheme

2.9 Flexural Plate Wave (FPW)

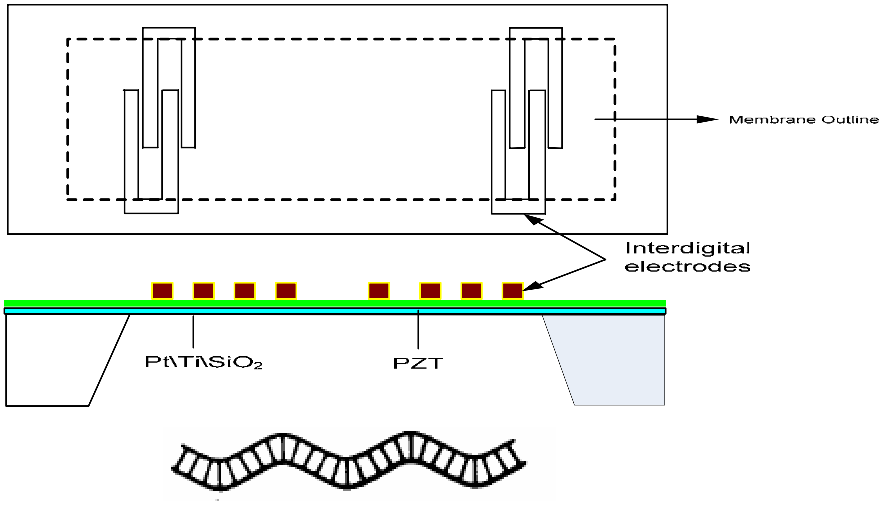

Figure 2.7 Schematic of the Flexural Plate Wave Device (a) Plan View, (b) Cross Section and (c) Flexing Wave Motion of the Membrane in a FPW Device

Figure 2.7 illustrates plan view, cross-section and the flexing motion of the membrane of an FPW upon excitation. Flexural Plate Waves are excited in thin membrane or plate whose thickness is smaller compared to the acoustic wavelength. The amplitudes of displacements associated with a flexural wave for a given power are large compared to other acoustic devices. The particle displacements are symmetrical to the ground plane. In this device, platinum is used as the ground.

2.10 Comparison: SAW Vs FPW

1. The higher operating frequency of the SAW complicates the oscillator circuit while the convenient operating frequency and the comparable wave velocity of the FPW allow an easy design of the electronic circuits.

2. The confinement of acoustic energy in an ultra thin membrane results in a very high mass sensitivity.

3. FPW device solves the problem of packaging by exposing the sensing area isolating the electronics part as they can be on different faces of the membrane.

4. The gravimetric response of the FPW is higher than a SAW due to increase in mass per unit area of the membrane on absorption. The sensitivity is generally two orders of magnitude higher than SAW devices.

5. The velocity of the flexural waves is smaller than the compressional fluid velocity which renders it a suitable choice for fluid loaded sensing.

6. The amplitude of the flexural wave is much high compared to their counterparts. The energy efficiency increases as the waves doesn’t travel deep into layers

7. The phase velocity for the FPW decreases as the ratio of membrane to the acoustic wavelength decreases.

2.11 Disadvantages of FPW Devices

Generally, the complexity involved in the fabrication of ultra thin membranes makes them a secondary choice when compared to SAW devices. The development of MEMS processing techniques makes the fabrication of these structures less of a challenge. The inherent fragile nature of the device requires a robust packaging scheme. Though this is a problem similar to QCMs it is easily overcome in FPW as the device is made with a frame that allows easy handling.

2.12 Generation of Flexural Wave

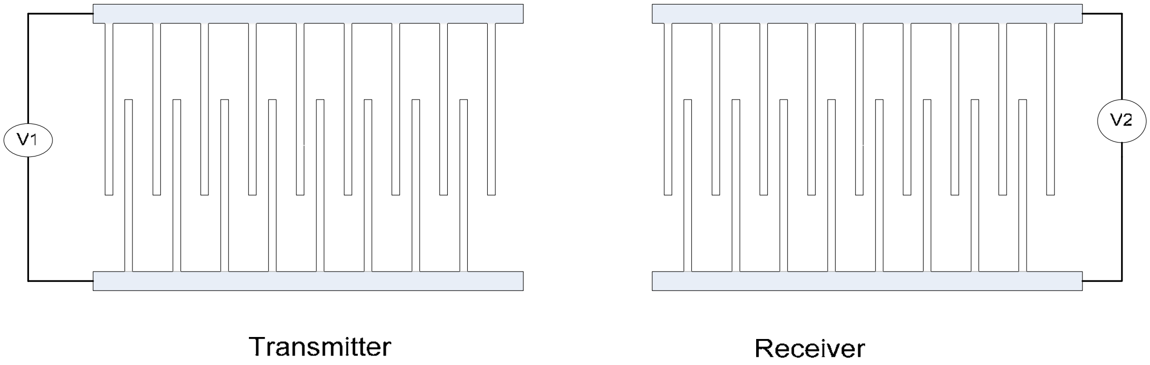

Figure 2.8 Schematic Depicting Transmitter and Receiver IDEs

Figure 2.8 represents the transmitting and receiving IDE's. Waves are generated by the Interdigital Electrodes (IDE) that is fabricated on top of the composite membrane. Inter digital electrodes are an array of finger shaped structures which are overlapped and interspersed [10] to generate waves. Generally these devices are configured as two-port devices. The alternate metal lines are connected to form the one-terminal driving point.

When a voltage is applied across the transmitter point, a periodic field is imposed on the crystal. On application of a sinusoidal field, a periodic strain field is created (obeying the converse piezoelectric effect.) which in turn gives rise to a standing surface acoustic wave. The wave perpetuates [1] itself in both the directions with the wavefront parallel to the transducer fingers. The traveling wave excites the receiver IDE’s (piezoelectric effect) and the current induced is measured as the output.

The propagation of a mechanical wave in a piezoelectric medium is accompanied by a wave potential. When the wave is incident on a conducting electrode, the wave potential is transformed into an external current. Figure 2.9 shows a schematic of the deformation caused by the IDE’s resulting in periodic wave generation.

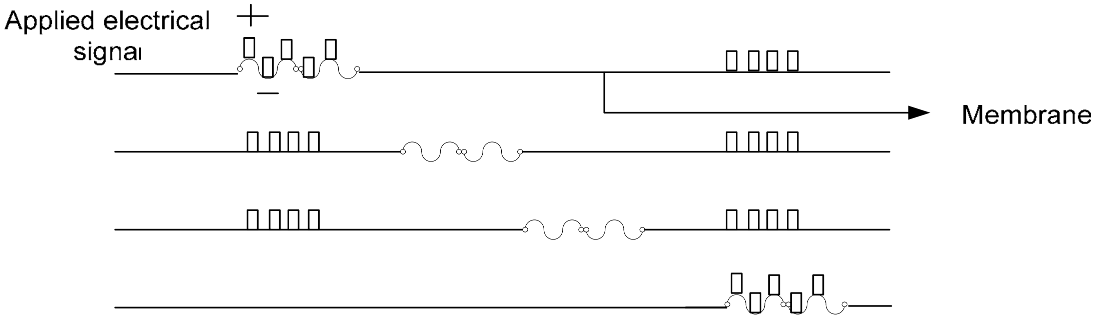

Figure 2.9 Working of the IDEs

Table 2.1 presents the IDE design specification dependence on the FPW device performance. Figure 2.10 defines the aperture and finger width of the IDEs.

Table 2.1 IDE Design Constraints on the Performance of the FPW Device

IDE Parameters	Dependent FPW Performance
Width of the IDE (b)	Frequency response
Spacing between IDE(d)	Operating Frequency
Aperture width or Overlap(w)	Effective impedance
Distance between transmitter and receiver	Phase delay
No of IDEs	Bandwidth

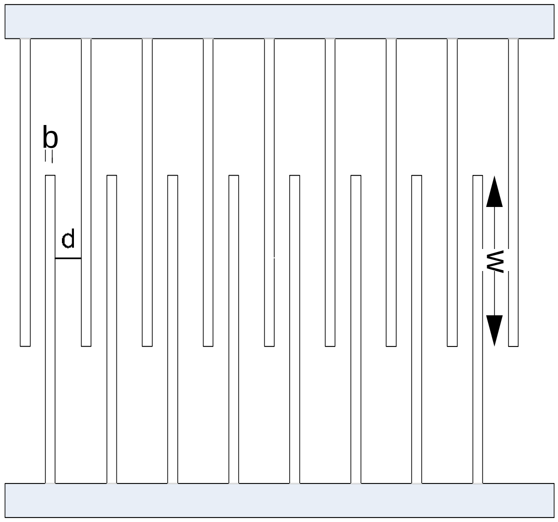

Figure 2.10 A Single IDE [36]

2.13 Mass Loading

The propagation of an acoustic wave is associated with two renowned effects namely the mechanical deformation and the electrical potential. When these devices are used for sensing, an active film (sorbent layer) is selectively coated between the IDTs or in the membrane. The interaction of the analyte with the chemically active thin film during the propagation of a mechanically deformed wave causes a frequency shift detected by oscillator circuits. The frequency shift is proportional to the incremental mass due to the interaction of the target species.

Equation governing the mass loading effect [1] is as follows:

$$s_m = -0.5((M+\rho sds))^{-1} \ldots (5)$$

Where,

s_m – Mass sensitivity ($m^2 \backslash g$)
M – Mass\Unit Area ($g \backslash m^2$)
ρs – Density of the active film($g \backslash m^3$)
ds – Active film thickness (A)

The common platform on which all these acoustic devices are built is the piezoelectric layer. In the next chapter, piezoelectric materials used for the fabrication of flexural plate wave devices will be discussed.

Chapter 3

Choice of Piezoelectric Material for Flexural Plate Wave Device

This chapter concentrates on the requirements of a piezoelectric material for high performance flexural plate wave devices. The reason for the choice of PZT as a piezoelectric material is substantiated. Various methods of depositing PZT are discussed and the suitability of sol-gel method is highlighted.

3.1 Requirements of Piezoelectric Material

In general, piezoelectric materials can be sub-classified into materials possessing ferroelectric and non-ferroelectric properties. Ferroelectric crystal structures have a direction of spontaneous polarization (polarization within a single ferroelectric domain in the absence of an external electric field) which is further enhanced by applying an electric field at an elevated temperature. As a result an accrued effect is obtained with a net piezoelectric response Eventhough, many non-ferroelectric materials possess non-centrosymmetric crystal structure (i.e., unequal spacing of atomic dipoles) their single crystalline nature prevents spontaneous polarization. Hence ferroelectric materials are known for higher piezoelectric properties.

Piezoelectric material develops a polarization (i.e., dielectric displacement) in response to an applied stress. The measure of piezoelectric response or the strength of a piezoelectric material is determined by the degree of non-centrosymmetry in the crystal structure. Application of an electric field along certain orientation causes a proportional strain in more than one crystallographic direction. The relation between electric field and strain, applied stress and dielectric displacement are specific to the orientation of the crystal. Generally the strain magnitude is found to be higher for the c-axis of the crystal.

Another critical parameter of interest is the Curie temperature (T_c).It is defined as the temperature above which a material loses its spontaneous polarization and becomes paramagnetic. Application of piezoelectric materials as sensors and actuators require high Curie temperature. This is mainly due to the various thermal processing steps involved in microfabrication.

The next criteria for the selection of the material, is the piezoelectric property of the material. As a step by step progress towards identifying the parameter, the direction of expansion and contraction of the piezoelectric material upon electric field must be understood. Figure 3.1 schematically explains the variation between the two stages.

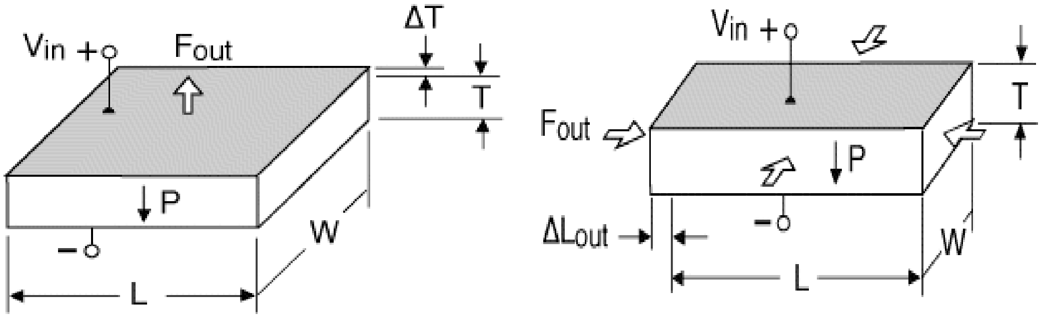

a. b.

Figure 3.1 Two Stages of Wafer (a) Longitudinal Wafer (b) Transverse Wafer [11]

Assume a piezoelectric disc of length ‘L’ and width ‘W’. When an electrical field (V_{in}) having the same polarity and orientation as the original polarization field (P) is placed across the thickness (T) of a single piezoelectric disc, the piece expands (F_{out}) in the thickness (ΔT) or "longitudinal" direction (i.e., along the axis of polarization) and contracts (F_{out}) in the transverse (ΔL_{out}) direction (i.e., perpendicular to the axis of polarization). By reversing the electric field, a contrary effect is observed.

3.1.1 Definition of Piezoelectric Coefficient

The behavior of piezoelectric materials is dictated by their piezoelectric coefficients. Piezoelectric coefficient (‘d’) is defined as the charge generated (Q) for an applied stress (F) and the unit being Coulomb per Newton.

$$d = Q / F \ldots (1)$$

It is a vector quantity generally denoted by d_{ij}. The first value (i) in the subscript represents the axis of initial polarization. The second value (j) relates to the axis of applied stress or strain. Figure 3.2a and 3.2b illustrates the difference between d_{33} and d_{31} modes respectively.

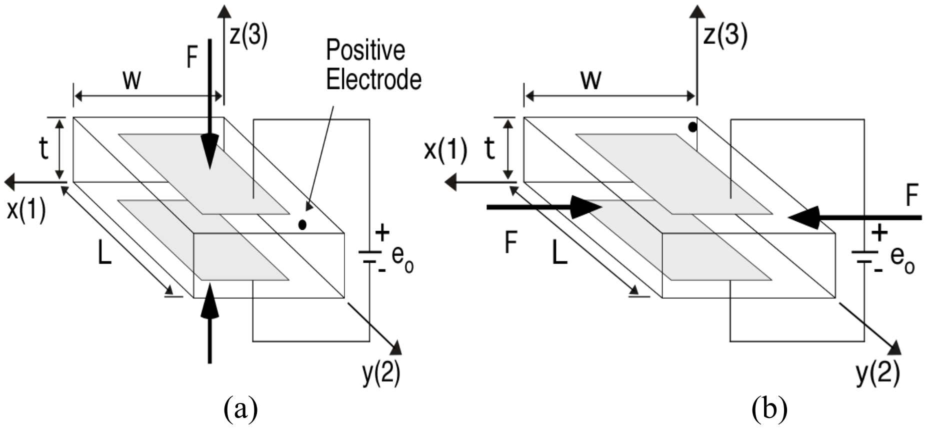

Figure 3.2 Types of Mode (a) d_{33} Mode (b) d_{31} Mode [11]

Consider a piezoelectric disc of length ‘L’, width ‘W’ and thickness ‘t’ placed along the crystal axes a(x), b(y) and c(z). The disc is excited by a voltage e_0 resulting in either a longitudinal or transverse strain (F). Taking into the account the previous discussion on maximum polarization axis and referring to the d_{33} schematic, the top electrode and the resultant strain is parallel to the z(3) axis in which the initial polarization tensor is positioned. This results in a longitudinal strain. On the other hand, referring to d_{31} schematic, the top electrode and resultant strain is parallel to the x (1) axis and perpendicular to polarization tensor in the z-axis. This results in a transverse strain. Figure 3.3 explains the different modes of excitation inherent in acoustic devices.

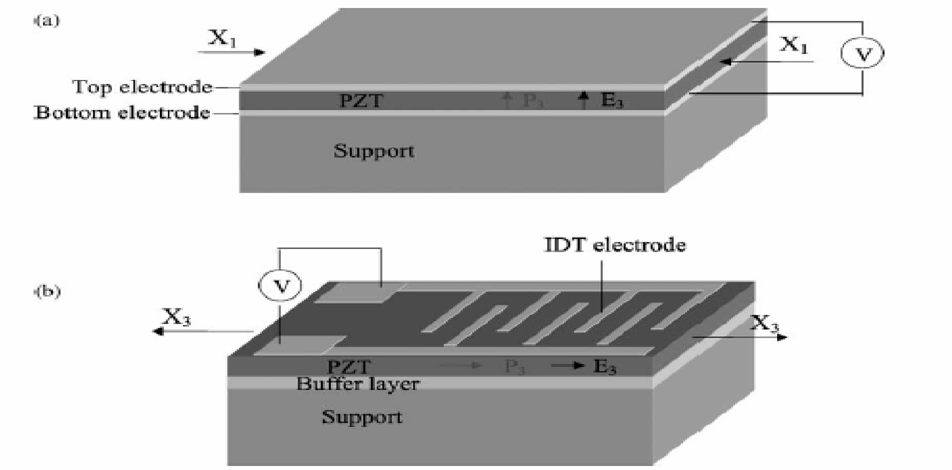

Figure 3.3 Different Modes of Excitation (a) d_{31} Mode (b) d_{33} Mode [12]

Consider an acoustic device with PZT as the piezoelectric material. Commonly used piezoelectric materials have d_{31} coefficients higher than other modes. Hence the acoustic devices are operated in the d_{31} mode when used as an actuator. The in-plane strain X_1 in the PZT, induced by the electric field E_3 is parallel to the remnant polarization P_r. Hence the film contracts laterally, making the vibrating structure i.e., the membrane on the PZT surface to flex in the upward direction. When the membrane bends in the upward direction, the PZT expands laterally with E_3 and anti-parallel with P_r, bending the membrane down. However when the applied electric field is large compared to coercive field of PZT, repoling takes place making E_3 again parallel with P_t. The electromechanical coupling factor which is used as a benchmark to compare piezoelectric materials is directly proportional to the d_{31} component. A higher value of coupling factor indicates large actuation force and high efficiency of transduction. As a concluding remark on the above discussion, certain requirements of a piezoelectric material have to be satisfied to obtain high performance flexural plate wave devices. They are,

1. Stable c-axis orientation
2. Ferroelectric in nature
3. Higher Curie temperature
4. Large d_{31} coefficient

Some of the earlier reported piezoelectric materials for the fabrication of flexural plate wave devices include ZnO [13], AlN [14] and PZT [15].The next section focuses on the relevance of these materials for the intended application.

3.2 Zinc Oxide (ZnO)

Zinc Oxide is a polar material that exhibits different properties based on the conditions of sputter deposition. It can act as semiconducting, piezoelectric and conducting material depending upon the sputtering parameters. Appropriate selection of processing conditions lead to highly preferred c-axis orientation. However, zinc oxide is a non-ferroelectric material with low remnant polarization and coercive field values, required for better actuation. The Curie temperature is just above room temperature which makes it incompatible to high temperature processing. Doped ZnO is under research for improving the Curie temperature. Zinc oxide is very sensitive to surrounding temperature and highly reactive to water, acids and bases. It generally requires a passivation layer as a measure of isolation from immediate environment. Due to its processing incompatibility, heavy dependence on processing conditions and stringent requirements makes it a moderate choice for piezoelectric applications. Since the polar axis cannot be re-aligned, the d_{31} and electromechanical coupling factors are poor. These find applications as IR detectors due to the hexagonal phase stability and high temperature sensitivity.

3.3 Aluminum Nitride (AlN)

Aluminum Nitride requires tedious process development in order to get an enriched orientation in the c-axis. The most attractive property is its high acoustic velocity of about 6000m/sec, which is nearly 10-15 times the value of PZT. The electromechanical coupling factor is much lower than ZnO. They are chemically inert and compatible with high temperature processing. The endurance against humidity makes it suitable for commercial non-hermetic packages. AlN posses high Curie temperature of about 130^0 C. AlN finds extensive application in bulk acoustic wave resonators (BAR) and mobile communication operating at GHz range. Due to the rugged nature and chemical inertness of this material, it is widely accepted in the CMOS industry for monolithic integration.

3.4 Lead Zirconate Titanate (PZT)

PZT is a ferroelectric material which possesses excellent piezoelectric properties. The d_{31} and electromechanical factors are at higher magnitudes than their counterparts ZnO and AlN. The c-axis orientation can also be tuned by changing the texture of the material. It also exhibits high Curie temperature of about 385^0 C. By a method of selective doping, the piezoelectric properties can be altered for the required application. The issue of lead evaporation and contamination makes it a poor choice for CMOS processes. However, high coupling factor with good ferroelectric properties classifies them to be used in non-volatile memory chips, chemical and biological sensing.

The input electrical energy to the electrodes is converted into acoustic, mechanical and heat energy. The magnitude of heat energy is directly proportional to the dielectric loss of the piezoelectric material. This dielectric loss is translated as intrinsic signal-to-noise ratio when the efficiency of transduction is evaluated. The noise signal (current or voltage) imposes a huge restriction on the resolution of the output signal .The conductive nature of piezoelectric ZnO under an alternating field presents a very high dielectric loss. The advantages of PZT over other piezoelectric materials are high piezoelectric coefficient and hence excellent sensitivity with high resolution, high Curie temperature indicating its stability, application specific tunability of piezoelectric parameters. The disadvantages of using PZT are the toxic nature of lead vapors during processing and higher fatigue. The structure of PZT is analyzed to account for the high d_{31} coefficients.

3.5 Crystal Structure of PZT

PZT has a Cubic Perovskite Crystal Structure (CPCS) represented by the empirical formula ABO_3. The lead (A) cation occupies the corners of the cube and Zr\Ti cation occupies the centre of the cube surrounded by octahedron of oxygen anions. Figure 3.4 illustrates the crystal structure of PZT.

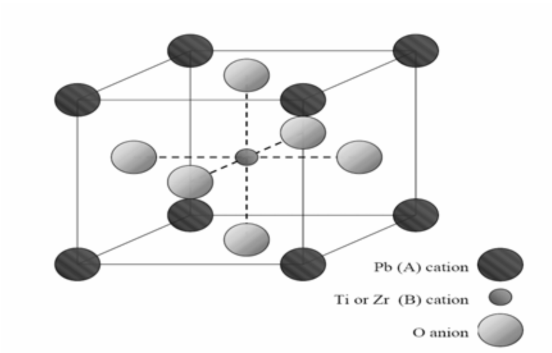

Figure 3.4 Crystal Structure of PZT [16]

The excellent ferroelectric behavior of PZT is attributed to the distortion of the CPCS due to the mobility of the cations (B) with respect to the oxygen atoms creating dipoles and the poling phenomenon. The analytical expression [16] to support the hypothesis is as follows;

$$T = R_a + (Ro/1.414 \ x \ (R_b + R_o)) \ \ldots \ (2)$$

Where T is referred to as the mobility factor, R_a represents the radius of the ‘A’ cation; R_b represents the radius of ‘B’ cation and R_o representing the oxygen atoms. Figure 356 shows the sketch of the crystal structure before and after poling. The polycrystalline anisotropy of PZT is further enhanced by poling.

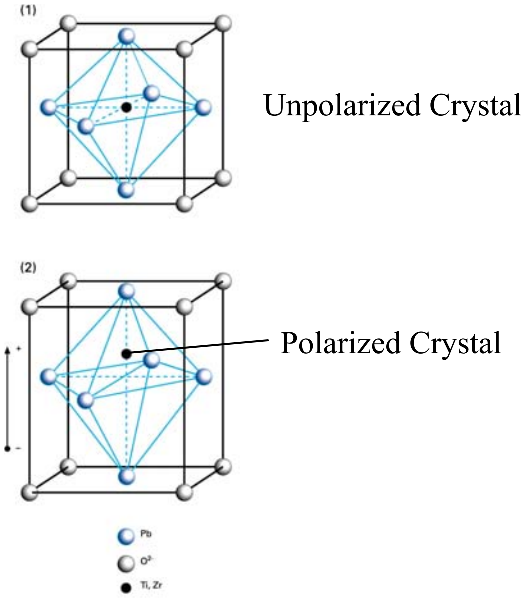

Figure 3.5 Crystal Structure Before and After Poling [11]

The three main sub-phases of the cubic perovskite are:-

1. Ti rich composition (>48%) - Tetragonal phase dominates
2. Zr rich composition (>52%) - Rhombohedral phase dominates
3. A peculiar 48\52 composition (Ti\Zr)-Morphotropic Phase Boundary (MPB)-Both tetrahedral and rhombohedral phase co-exists

Figure 3.7 illustrates the phase transformation at the morphotropic phase boundary. In a PZT crystal structure, there exist lead titanate and lead zirconate ($PbTiO_3$ or $PbZrO_3$) as partial compounds corresponding to the tetragonal and rhobohedral structures. Based on the composition either one of them dominates. At morphotropic phase boundary, both these compound co-exist giving rise to phenomenal ferroelectric properties. The phase diagram of PZT is shown in Figure 3.8.

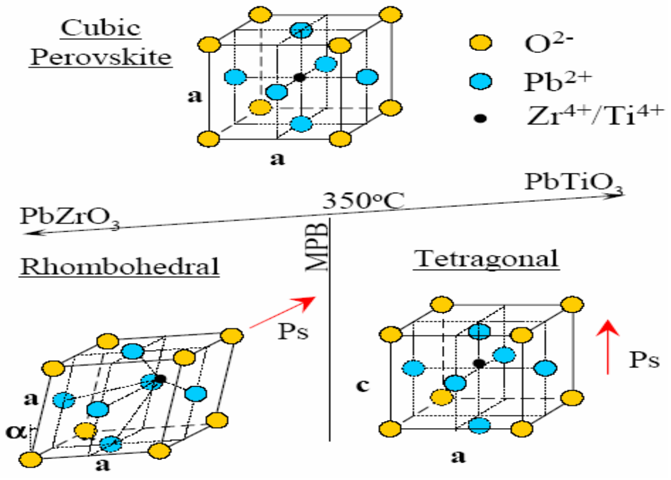

Figure 3.6 Phase Transformation at the MPB [17]

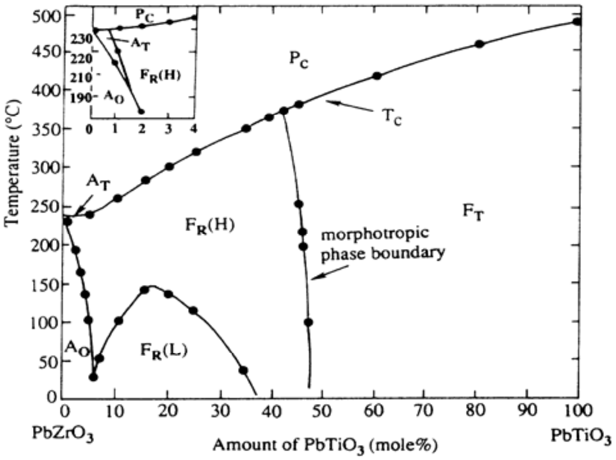

Figure 3.7 Phase Diagram of PZT [18]

3.6 Methods of Depositing PZT

Thin film PZT can be deposited through various techniques, like metal organic chemical vapor deposition (MOCVD) [19], sputtering [20], pulsed-laser ablation (PLA) [21] and chemical solution deposition routes (Sol-gel) [22]. A comparison of each technology for the selection of the best deposition scheme is shown in Table 3.1.

Table 3.1 Comparison of Various Methods of PZT Deposition

Parameters/Method	MOCVD	Sputtering	PLA	Sol-gel
Principle	Layer deposition of desired atoms due to chemical reaction between organic gaseous precursor and substrate	Bombardment of target atoms using gaseous ions driven by plasma	Material removal by bombarding the surface of the target with short energetic pulse of focused laser beam	Metal-organic decomposition of precursors under heat treatment to form crystallized gel structure
Uniformity	Conformal	Good	good	moderate
Process Temperature	High	Low	Low	Moderate
Composition and Stoichiometry	Poor	Good	Moderate	Excellent
Deposition Rate	High	Low	High	Low
Wafer Coverage	excellent	Very good	Good	excellent
Cost	High	Low	High	Moderate
Manufacturability	Large Scale	Small scale	Large scale	Small scale
Ease of Fabrication	Complex	Simple	Simple	Moderate
Process Variables	Temperature, Pressure and Precursor Concentration	Power, Pressure, Type of Plasma, Substrate Temperature	Laser Frequency, Laser Energy, and Substrate Temperature	Type of Solvent, Processing Conditions, and Precursors

The objective of this thesis is to fabricate a highly sensitive flexural plate wave device. This requires a precise orientation and stoichiometry of the piezoelectric material for enhanced piezoelectric properties. Sol-gel offers excellent control over the stoichiometry and texture of the PZT thin film in spite of its low deposition rate and non-uniformity.

Chapter 4

Influence of Sol-Gel Processing Conditions on Structural Evolution of PZT

This chapter presents the basic steps and processing conditions involved in a sol-gel process. The texture, morphology and structural evolution of PZT as a function of processing conditions are discussed. A brief note on the conventional sol-gel process is presented. Finally, the process variations in sol-gel technique leading to enhanced texture and morphology of PZT are described. To put this discussion in perspective the structure of the FPW is illustrated below.

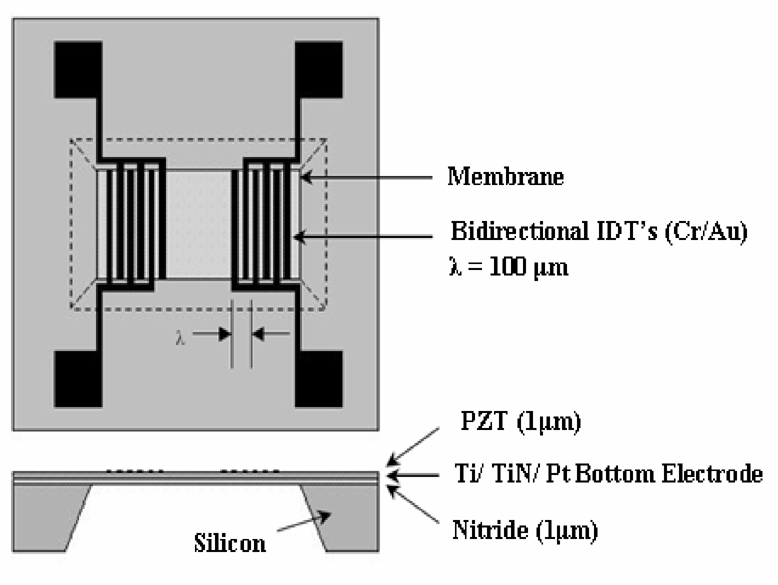

Figure 4.1 Material Layers in a FPW [7]

Figure 4.1 schematically illustrates the material layers in the FPW. The structure comprises of a Si wafer coated with an adhesion layer, a diffusion barrier a bottom electrode, then the sol-gel PZT layer followed by the top electrode. As the entire structure is developed with the aim of getting improved properties from sol-gel PZT, sol-gel process is discussed first.

4.1 Sol-Gel Process

Sol-gel methodology facilitates excellent compositional control and process tunability. Figure 4.2 illustrates the basic steps involved in sol-gel processing.

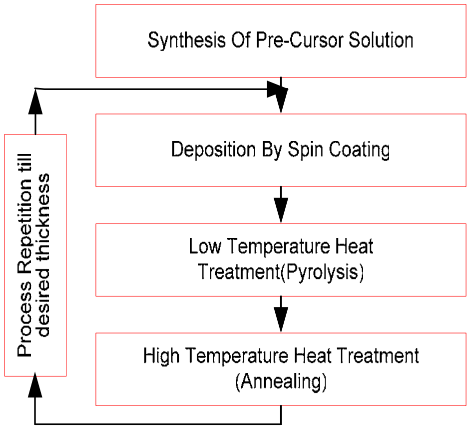

Figure 4.2 Basic Steps Involved in Sol-Gel Processing

As briefly discussed earlier, the Sol-gel method involves the synthesis (hydrolysis and condensation) of organometallic precursors required for subsequent processing. A suitable solvent is used to dissolve the complex metallo-organic alkoxides to form the sol. The precursors and solvents are selected based on the boiling point, viscosity and surface tension. A fundamental criterion for materials selection is that the solution should retain the chemical integrity of the components till the final step of annealing. The synthesized solution is then spin-cast onto the substrate. Initially, significant amount of organics are present in the as-cast films. It is necessary to remove the organic constituents from the film before the crystallization of the amorphous network, which otherwise would result in cracks in the film. For this reason the typical thickness that can be achieved per spin needs to be under 0.1µm. The semi-volatile organic compounds present in the solution are removed through pyrolysis. Pyrolysis is generally carried out at 355^0C in an open atmosphere after initial drying of the spun-cast film at around 100^0C. The drying removes most of the solvent from the film by evaporation, leaving the film solid, which is still porous in nature. Finally the gel to ceramic conversion takes place through a high temperature annealing treatment in desired ambient. This high temperature firing results in crystallization and densification of the structure. Finally, the stoichiometry of the product is determined, and its properties are measured to optimize the process conditions.

4.2 Influence of Sol-Gel Parameters and Processing Conditions on Texture and Morphology of PZT

Even though the sol-gel method seems to be a simple process, it does possess a number of variables and constraints allowing exploitation of its unique features. These mainly stem from the volume of organic content involved that may result in cracking on high temperature processes. As can be envisioned, significant weight loss and shrinkage occur in the film during thermal stages. Hence, a careful control on these parameters, processing conditions is required and their influence on the final structure is understood to minimize the issues.

The critical parameters and processing conditions that determine the texture and morphology of sol-gel PZT include 1) the choice of bottom electrode, 2) annealing temperatures of bottom electrode, 3) type of buffer layer, 4) choice of solvent, 5) pyrolysis temperature, 6) annealing mode, 7) stoichiometry and 8) annealing module for crystallization during final stages.

4.2.1 Bottom Electrode

Numerous materials have been researched upon for the choice of bottom electrodes. However, only two types are the most popular. They are the conducting oxide electrodes [23] and platinum electrode. PZT films crystallized over Pt surface with Ti as the adhesion layer, result in increased (111) orientation. This phenomenon can be explained in terms of excellent lattice matching between the oriented Pt film and PZT structure. When iridium oxide was used as a bottom electrode [23], the final PZT structure exhibited multi-phase texture involving the defective pyrochlore stage. Hence the ferroelectric properties of Iridium Oxide/PZT were poor. The major advantage of using IrO_2 is that it minimizes fatigue in PZT thin film. Ruthenium oxide has also been used as a bottom electrode [24]. It produces PZT with high intensity secondary stages and inhomogeneous morphology. Hence Pt has been used as a bottom electrode in this research.

4.2.2 Annealing Temperatures for Bottom Electrode

The Platinum film acting as a bottom electrode has a larger thermal coefficient of expansion than the PZT or the substrate. This mismatch leads to stresses being induced build up during the subsequent heat treatments of PZT. The total stress contribution can be sub divided into 1) stress due to intrinsic effects and 2) thermal mismatch. The intrinsic stress arises from film contamination and incomplete structural ordering processes [25] that may occur due to film growth. Generally platinum is annealed prior to deposition of PZT, to improve its (111) orientation in order to obtain a well crystallized perovskite structure. This annealing step further induces stress on the platinum layer. On application of PZT, the stress prevalent in the annealed Pt decreases as the film is initially stretched and then shrinks following the heat treatment for the PZT layer (there is significant shrinkage in the PZT layers). The annealing temperature of any bottom electrode is chosen to serve two purposes: 1) Improve the degree of epitaxy of PZT films, enhancing the texture and 2) Minimize the difference in stress mismatch resulting in smooth morphology without hillocks.

4.2.3 Type of Buffer Layer

A buffer or seeding layer is used intentionally to drive the nucleation of the bottom electrode and thus the PZT towards a preferred orientation. The most commonly used materials are lead titanate ($PbTiO_3$) and titanium oxide (TiO). Use of $PbTiO_3$ [26] as a seed layer reduces the growth temperature of PZT. The PZT layer nucleates in the (100) direction. The unique behavior can be explained in terms of the ample nucleation sites available for the PZT grains to grow. However this method is characterized by low remnant polarization values. Titanium oxide is sputtered in-situ in oxygen ambient in a desired ratio with argon. In this case, PZT nucleates in the (111) direction. During the annealing stages, titanium crystallizes along Pt grain boundaries enriching the stoichiometry towards perovskite (111) structure. Hence Ti has been used as the buffer layer.

4.2.4 Choice of Solvent

The solvent used in sol-gel processing greatly influences the microstructural properties. Methoxy ethanol is widely used as a solvent due to its high reactivity and minimal aging effects. To improve the density of the film, solvent with lower molecular weight is used. Propylene glycol has a lower molecular weight and higher viscosity resulting in increased layer thickness per spin. Generally a solvent with moderate reactivity and viscosity is used. The intensity of (111) orientation increased as the molecular weight of solvent decreased. Considering these issues, Propylene glycol is used as the solvent in this process.

4.2.5 Pyrolysis Temperature

It is a very critical processing parameter which determines the preferential orientation of the thin film in its amorphous state. There is a shift in the crystal orientation from (111) to (100) when the material is pyrolized above the curie temperature of the material. Wen Gong et al. [27] found the competing mechanism in the growth (100) grains over (111) orientation. When the pyrolysis temperature is below 400^0C, a dominant (100) orientation is observed. However, PZT film tends to show a strong nucleation in (111) orientation for temperatures between 200 and 380^0C. Formation of PZT (111) oriented grains has been attributed to the low interfacial energy between the piezoelectric layer and bottom electrode. At temperatures above 400^0C, PZT disassociates itself to form PbO seeds which acts as seeding layer on top of the bottom electrode to form PZT (100) grains. The amount of lead loss is also taken into consideration while deciding the pyrolysis temperature.

4.2.6 Annealing Mode

The PZT film is annealed either using a tube furnace or a rapid thermal annealing (RTA) set-up. The use of tube furnace induces secondary and unwanted intermediate fluorite/ pyrochlore phase, detrimental to both electrical and piezoelectric properties of the thin film. Rapid thermal annealing of films kinetically delimits the favorable intermediate growth by surpassing the growth temperature. However a tube furnace ensures uniform heating profile across the wafer. The film tends to crack and peel in a RTA if the suitable temperature is not maintained. Hence a RTA with a carefully optimized annealing cycle is used to transform fully from an amorphous phase to polycrystalline state.

4.2.7 Stoichiometry

Apart from the pyrolysis temperature, the Zr/Ti ratio and lead content before annealing play significant roles in determining the orientation of the final ceramic. The Zr/Ti ratio factor is one of the indications of the dominance of phases determining the ferroelectric nature of the PZT. Higher zirconium content in the film before annealing results in larger grains favoring the fluorite configuration during the annealing process. Basically a higher Zr [28] slows the crystallization process of transforming into a perovskite structure whereas higher titanium content forces the onset of perovskite crystallization at lower temperatures.

The lead content in the PZT film at each processing stage is very critical to the formation of the final perovskite structure. The evaporation of lead during high temperature processing is unavoidable. A rule of thumb is to have excess stoichiometric lead in the precursor addition stage. The loss of lead oxide leads to degradation of the film. Inclusion of excess lead results in dense grain structure reduced in size, lower crystallization temperature and Ti rich phase enhancing the texture of (111) orientation.

4.2.8 Annealing Module for Crystallization

Direct conversion from the amorphous stage to the perovskite structure is a thermodynamically unstable phenomenon. Hence careful choice of the transition temperatures is necessary to avoid peeling and cracking of the film. Generally the perovskite structure is formed at around 700^0C. Lower temperatures enhance the formation of the spurious phase. The final perovskite is achieved by passing through intermediate stages for very short intervals of time to ensure stress mismatch and growth mechanism tolerance. Annealing time and flow of annealing ambient are critical to the morphology of the film. Lesser annealing times lead to (100) and secondary phase domination while longer annealing times degrade the film quality. Oxygen is used as an ambient to crystallize amorphous PZT as the oxygen content in the final structure is one of the factors determining the ferroelectric properties of PZT. A deficit of oxygen produces poor quality films with degradable properties. On the other hand, excess oxygen results in blisters and generates excess stress in the film to peel off.

4.3 Company Standard Sol-Gel Processing Conditions

Process steps in an industry standard sol-gel solution (Mitsubishi^{TM}) are presented below. Figure 4.3 [29] illustrates the flow chart recommended to produce 1µm thick films.

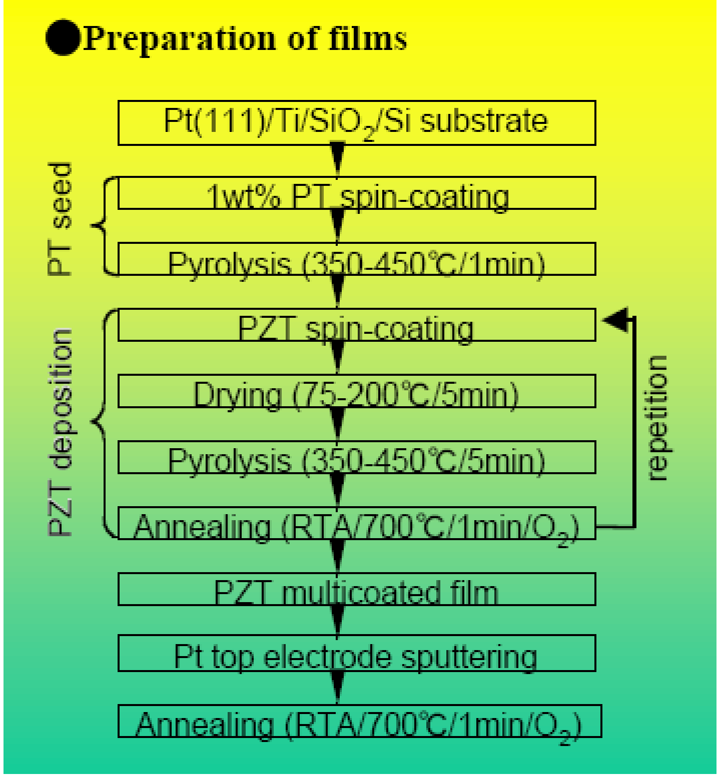

Figure 4.3 Process Flow to Achieve 1µm Thick PZT Films [29]

Lead Titanate is used as a seed layer. An additional pyrolysis step is performed after depositing the seed layer. The second stage pyrolysis is a two step process. In the first step, light material like water gets evaporated and then volatile organics are evaporated. The second step called the densification stage is a direct process with a temperature setting equal to the crystallization temperature of PZT. Figure 4.3(a) and 4.3(b) illustrates the cross-section of PZT and P-E curve of 1.5µm thick PZT layer made using this process.

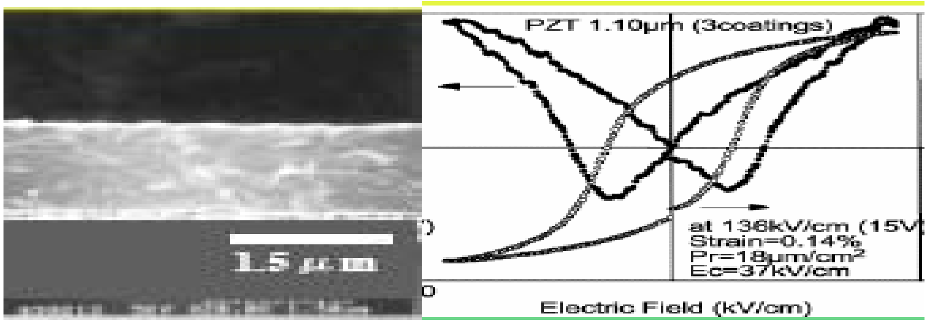

Figure 4.4 Salient Features of Mitsubishi TM PZT Solution (a) Cross Section of PZT Layer (b) Hysteresis Curve of PZT [29]

The cross section of the PZT layer appears to have columnar growth with remnant polarization (P_r) of 20µC/cm^2 and a coercive field of 37KV/cm. The ferroelectric values appear to be low, indicating the suppressed (111) phase when compared to (100) phase.

4.4 Need For Sol-Gel Process Optimization

The demand for high sensitivity flexural plate wave sensors and actuators has driven the need for materials with good piezoelectric properties, a function of crystal orientation. Sol-gel offers excellent process tunability tailoring to the needs of specific application. Several research papers have been published [30], [31] reporting an improvement in the texture and morphology of sol-gel derived PZT which enhances the preferred orientation.

4.5 Process Optimization

In this work, the following modifications led to the optimization of the sol-gel processing conditions. Unless and otherwise stated, the PZT solution used is procured from Mitsubishi^{TM}.

1. Smooth transition in the annealing temperature of the bottom electrode to satisfy stress mismatch and improve epitaxy of the PZT film. The bottom electrode is chosen to be Ti/TiN/Pt. It is annealed in a programmable rapid thermal annealer with precise control over the ramp rate. The transition temperatures are 450^{0}C, 600^{0}C and 700^{0}C each a minute at a ramp rate of 40^{0}C/sec. Formation of the

intermetallic compound Pt_3Ti due to the above mentioned annealing conditions improves the pervoskite (111) orientation.

2. The spin speed and time of spin are designed to achieve a uniform coating of the sol-gel solution for homogenous nucleation while annealing. It’s a two stage spinning process starting with 500RPM for 5 secs and increasing to 2100 RPM for 60 secs.

3. Two different types of pyrolysis set up are used. Dual hot plate and multi zone pyrolysis gave much improved results than conventional processing standards. In dual hot plate set up, the wafer is slowly placed in a hot plate at 150^0C for a minute and then transferred to another at 365^0C for two minutes. Multi zone pyrolysis is carried out by holding the wafer at different heat zones while placing it in the hot plate at 365^0C for 2 min.The pyrolysis temperature is chosen based on the amount of lead loss and the Curie temperature of the material.

4. Rapid thermal annealing is used to crystallize and densify the film. It is executed in a similar fashion as that of the bottom electrode. The various annealing temperature stages are 450^0C , 650^0C and 750^0C each a minute at the ramp rate of 30^0C/sec.The temperatures are chosen based on several experimental trials with the inspection of the morphology of the film. The unique feature of these values were seen in terms of the formation of Pt-Pb intermediate compound which provides nucleation sites with low interface energy for the PZT(111) to grow. After every three spins, the film is pyrolized and then annealed at the above mentioned conditions. This procedure stabilized the pervoskite (111) phase suppressing the (100) phase. There was no defective phase formation at any stage of the annealing process.

5. The flow rate of O_2 is fixed at 40 SCCM based on the final stoichiometry and morphology of the film.

Chapter 5

Fabrication and Issues

This chapter concentrates on the development of a repeatable process flow in the fabrication of a flexural plate wave device. The issues encountered in each process step towards the progress of the final device and solutions devised are also discussed in detail. Figure 5.1 illustrates the complete process flow for the fabrication of sol-gel based PZT FPW device.

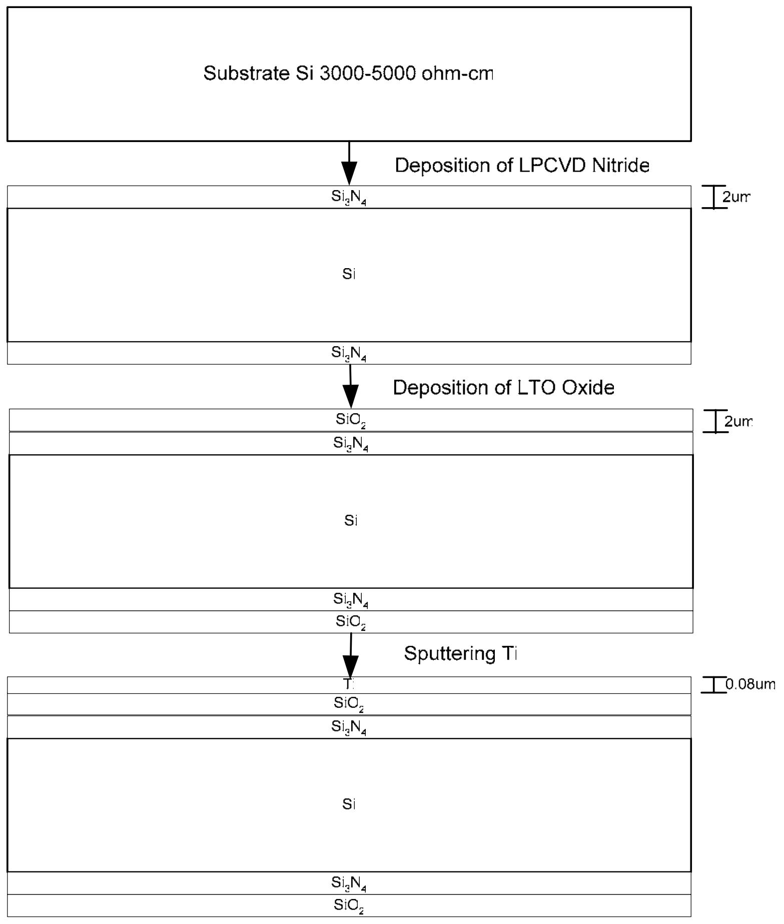

Figure 5.1 Complete Process Flow

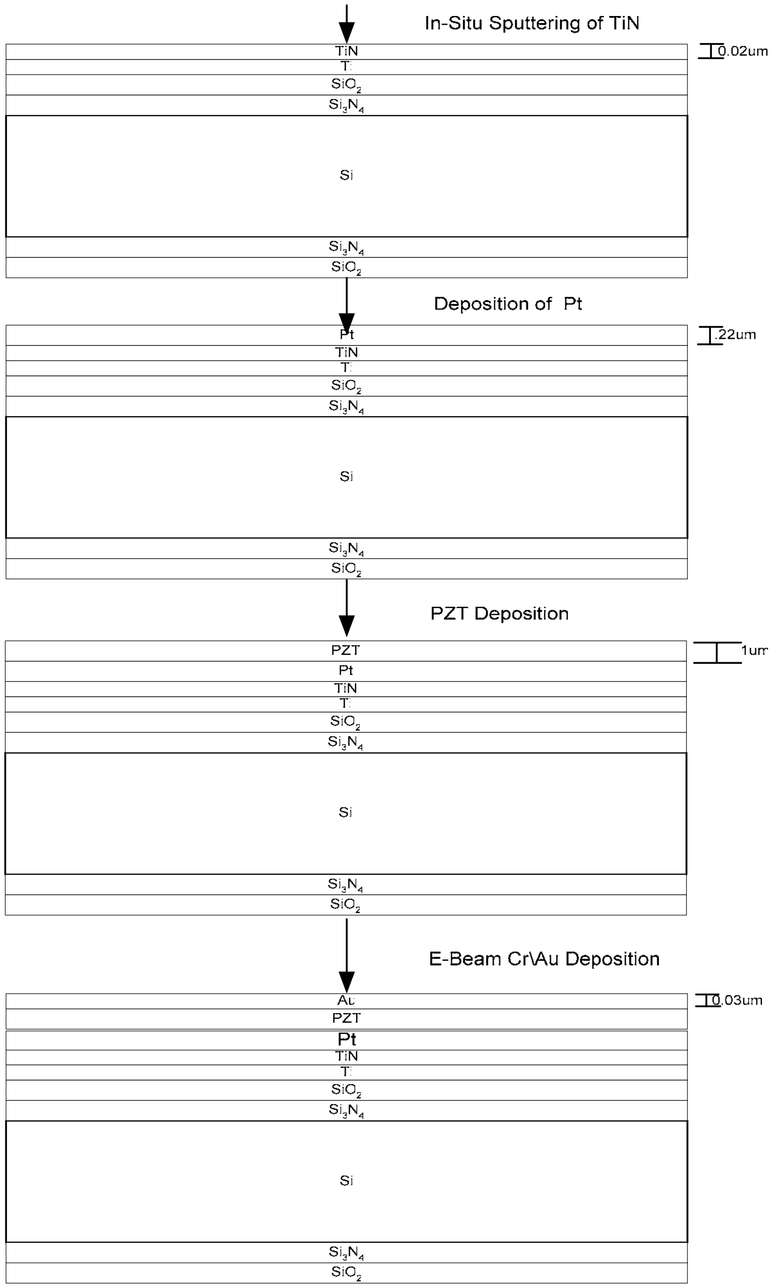
In-Situ Sputtering of TiN
TiN
Ti
SiO_2
Si_3N_4
Si
Si_3N_4
SiO_2
0.02um
Deposition of Pt
Pt
TiN
Ti
SiO_2
Si_3N_4
Si
Si_3N_4
SiO_2
.22um
PZT Deposition
PZT
Pt
TiN
Ti
SiO_2
Si_3N_4
Si
Si_3N_4
SiO_2
1um
E-Beam Cr\Au Deposition
Au
PZT
Pt
TiN
Ti
SiO_2
Si_3N_4
Si
Si_3N_4
SiO_2
0.03um

(Continued)

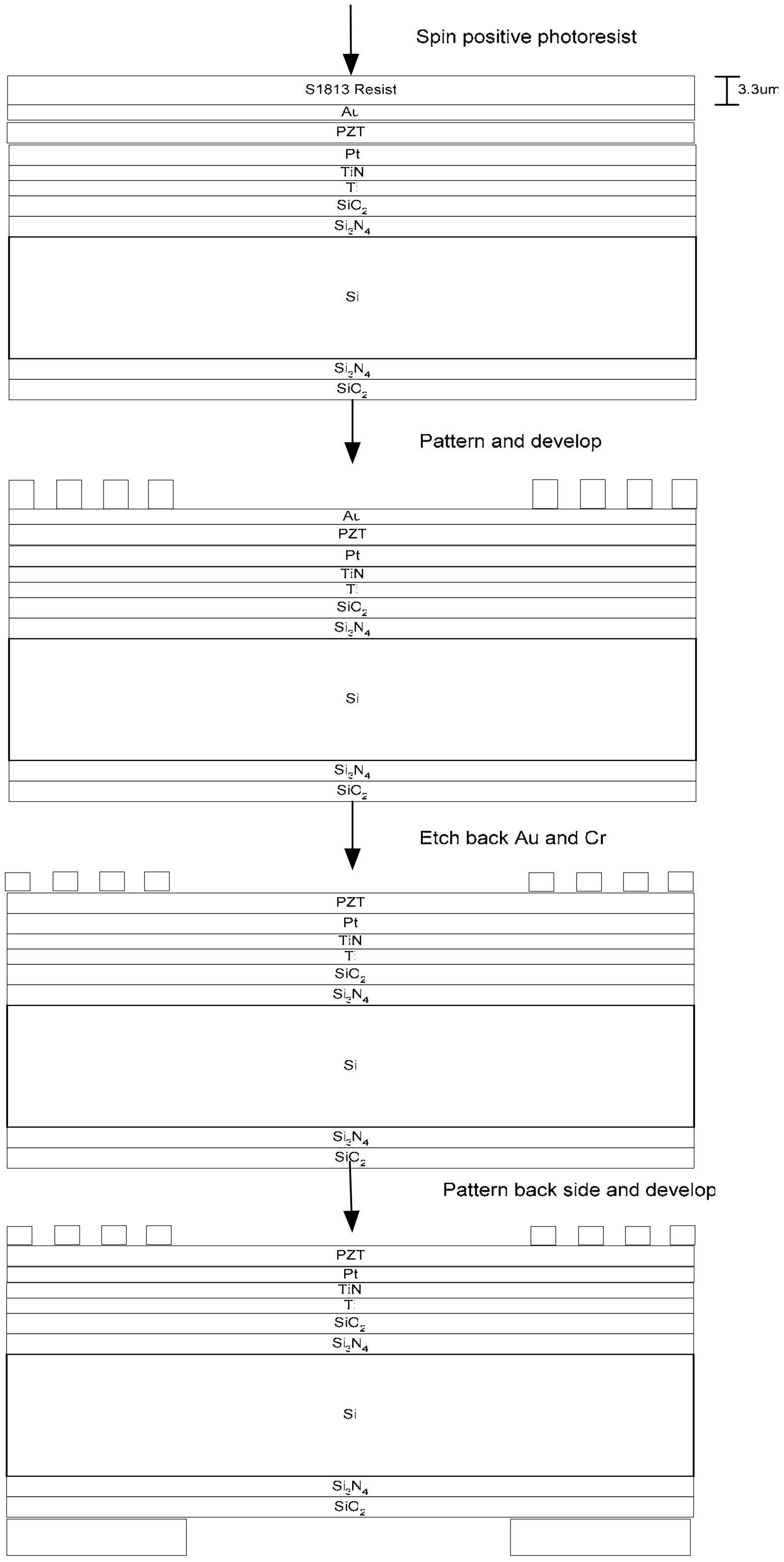
Spin positive photoresist
S1813 Resist
3.3um
Au
PZT
Pt
TiN
Ti
SiO$_2$
Si$_3$N$_4$
Si
Si$_3$N$_4$
SiO$_2$
Pattern and develop
Au
PZT
Pt
TiN
Ti
SiO$_2$
Si$_3$N$_4$
Si
Si$_3$N$_4$
SiO$_2$
Etch back Au and Cr
PZT
Pt
TiN
Ti
SiO$_2$
Si$_3$N$_4$
Si
Si$_3$N$_4$
SiO$_2$
Pattern back side and develop
PZT
Pt
TiN
Ti
SiO$_2$
Si$_3$N$_4$
Si
Si$_3$N$_4$
SiO$_2$

(Continued)

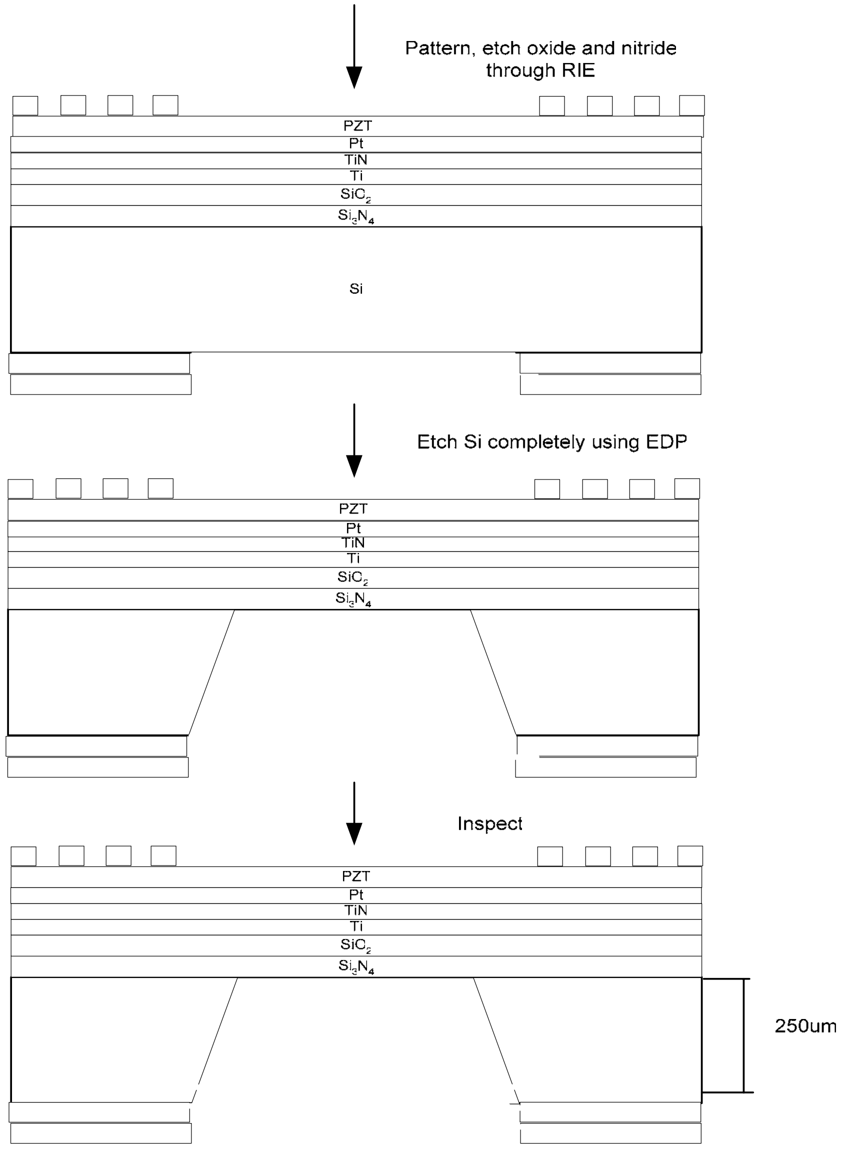
Pattern, etch oxide and nitride through RIE
PZT
Pt
TiN
Ti
SiC2
Si3N4
Si
Etch Si completely using EDP
PZT
Pt
TiN
Ti
SiC2
Si3N4
Inspect
PZT
Pt
TiN
Ti
SiC2
Si3N4
250um

(Continued)

5.1 Process Description

The process steps involved in the fabrication of FPW device are discussed in this section. Silicon Nitride is used as an etch stop layer and also as the membrane. Over the Si_3N_4 layer a low temperature oxide is deposited. The oxide layer is used to compensate the tensile nature of the Si_3N_4. It also acts as a hard mask for reactive ion etching (RIE) of nitride. Next the bottom electrode is formed by sputtering Ti/TiN and Pt.

The platinum layer is annealed in argon ambient using the RTA. The annealing cycle takes into account the thermal and stress mismatch during the densification stage of the PZT. The spin speed and pyrolysis parameters are altered to ascertain uniformity before the annealing steps. The annealing cycle for crystallization and densification of PZT is tuned to obtain a smooth morphology of the deposited PZT. The RTA wafer holder, designed for 4 inch wafers; are restructured to get a uniform heating profile over the 2 inch device wafers. Back side patterning is performed to open up etch windows on which RIE of nitride is done. Then the wafer was subjected to buffered oxide etch (BOE) to remove the oxide layer. Metallization of the interdigital transducers (IDTs) is carried out after patterning the front side using EVG mask aligner. A small portion of PZT surface is etched in BOE to contact the platinum layer which acts as the ground. The device is poled for ferroelectric domains to align for better performance.

The silicon substrate is etched using ethylene-diamine-pyrocatechol (EDP), an anisotropic etchant. A different experimental approach is adopted to etch silicon to reach the nitride. The periphery of the wafer is protected with Teflon tape. Another nitride wafer is attached to the device which acts as a mechanical support. A jig arrangement is used to prevent EDP from interacting with PZT. The etch rates of EDP are well characterized with prior experiments. After etching 200µm, the wafer is inspected every half an hour for the membrane thickness. After etching 2µm membrane the device is soaked in water with 2-isopropanol as a cleaning protocol and finally dried in oven.

5.2 Process Issues and Solutions

5.2.1 Change of Barrier/Etch Stop Layer from Si to Si_3N_4

Initially silicon membrane was chosen to be the vibrating structure due to its elasticity and fracture strength. Boron etch stop technique was used to fabricate the ultra thin membrane. This approach failed in implementation possibly because of (a) the constant degradation of boron concentration on high temperature processing and (b) the boron was diffused into the wafer, not implanted; hence the doping interface may not be sharp and concentration not high enough. This resulted in a through etch of silicon.

At present, silicon nitride is used as the membrane material. It is deposited by means of Low Pressure Chemical Vapor Deposition (LPCVD). The LPCVD nitride deposited has low stress and a pin-hole free profile. The thickness of nitride deposited depends on the sensitivity requirements of the device. Considering practical feasibility (handling) and allowing a tolerance margin, the thickness is fixed to be 2μm. A low temperature CVD oxide of similar thickness is deposited on top of nitride for stress compensation.

5.2.2 Modification of Bottom Electrode from Evaporated Ti/TiO/Pt to Sputtered Ti/TiN/Pt

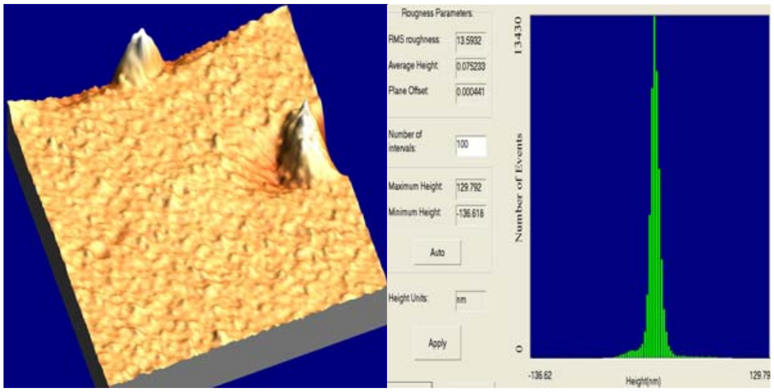

Rougness Parameters
RMS roughness: 13.5932
Average Height: 0.075233
Plane Offset: 0.000441
Number of intervals: 100
Maximum Height: 129.792
Minimum Height: -136.618
Height Units: nm

Figure 5.2 AFM Image of Ti Surface Annealed in Ar Ambient, Z-axis Scale Indicating 13nm Roughness

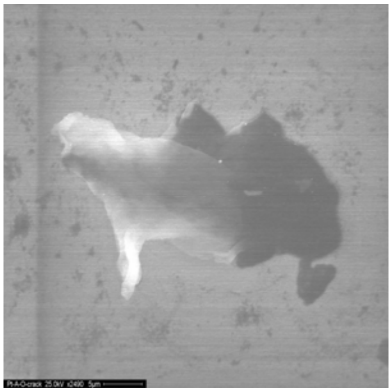

Figure 5.3 SEM (25KV, 2.4K) Image of a Hillock on Pt Deposition

The choice of bottom electrode is very critical to attain the right texture and morphology of the PZT layer. Initially, Ti/TiO_2/Pt was chosen as the bottom electrode. Titanium was deposited in an E-beam evaporator. The titanium layer is annealed in argon environment for the formation of TiO to act as a buffer layer. Significant undulations of roughness 13nm were still noted on the surface and confirmed by atomic force microscopy (AFM). Figure 5.2 shows an AFM image of the Ti surface annealed in Argon environment indicating a roughness of 13 nm. Figure 5.3 shows a SEM micrograph of a hillock piercing the Ti layer after Pt deposition. Even after annealing Pt, the intensity of platinum (111), favorable for the growth of PZT (111) was found to be low, which is confirmed by X-Ray diffraction (XRD) measurement. Figure 5.4 illustrates the XRD image for annealed platinum. Table 5.1 indicates the intensity of Pt (111).

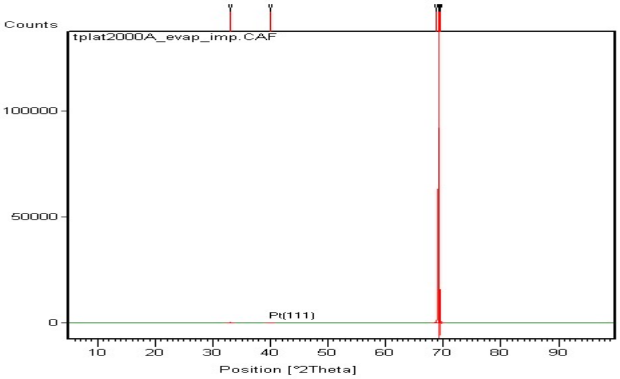

Figure 5.4 XRD Illustrating Pt (111) Intensity on Evaporation

Table 5.1 Evaporated Pt (111) Intensity on Annealing

Element	Pos. [°2Th.]	Height[cts]
Pt(111)	40.0503	137.62
Si(400)	69.129	92247.22

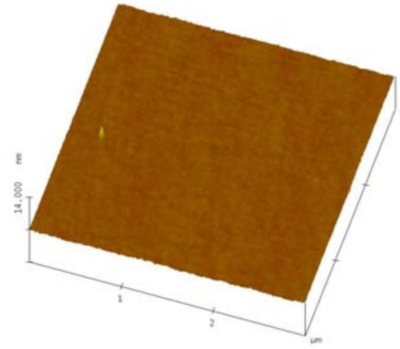

Figure 5.5 AFM Image of TiN Surface

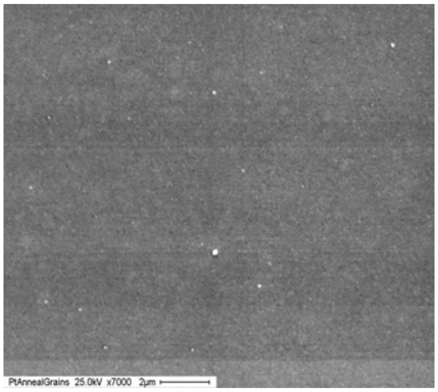

Figure 5.6 SEM (25K, 7K) Image of Annealed Pt Surface

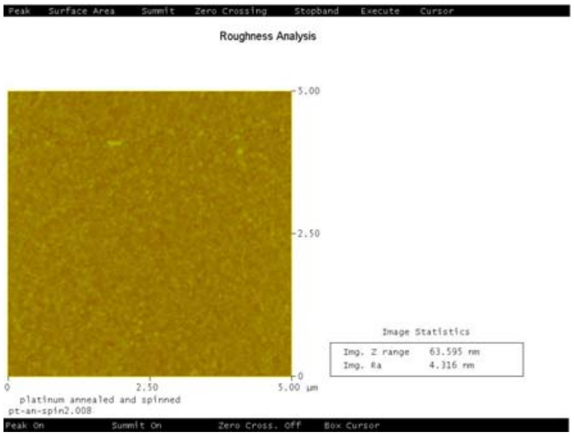

Roughness Analysis

Image Statistics

Img. Z range 63.595 nm
Img. Ra 4.316 nm

platinum annealed and spinned
pt-an-spin2.008

Figure 5.7 AFM Image of Annealed Platinum Surface

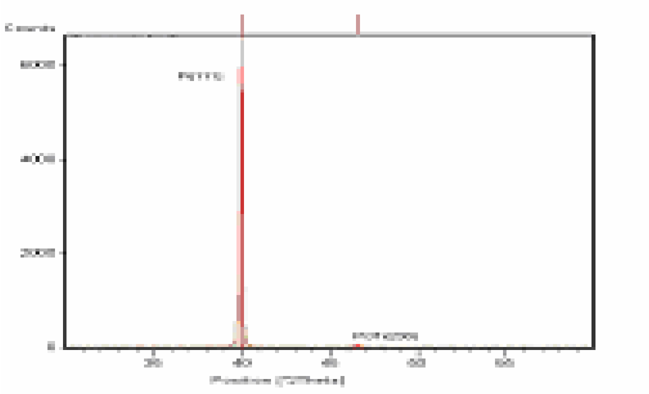

Figure 5.8 XRD Revealing Improved Crystallinity

Table 5.2 Sputtered Pt (111) Intensity on Annealing

Element	Pos. [°2Th.]	Height[cts]
Pt(111)	40.0503	5460.08
Pt_3Ti(111)	46.633	132.72

To overcome the previously discussed issues, the bottom electrode is changed from Ti/TiO_2/Pt to Ti/TiN/Pt. The bottom metal is used as the adhesion layer while the dielectric between the two metals is to prevent interdiffusion of the metals. The use of TiN as a barrier layer is well established in the interconnect industry. The ratio of metallization is maintained as Ti/TiN/Pt::2:0.2:1 to avoid interdiffusion of Ti into platinum and improve the texture of Pt (111). Initially, 80nm of Ti is sputtered using AJA sputter system at a working pressure of 1mTorr. Then, 8nm of Titanium nitride sputtered in-situ with nitrogen as the reactive gas. As this process is carried out without breaking vacuum, good adhesion is ensured. Figure 5.5 shows an AFM image of the TiN surface indicating a smooth morphology. It acts as a barrier to back diffusion of platinum. Platinum is sputtered at a working pressure of 2mTorr for a thickness of 220nm. The crystalline nature of platinum is improved by depositing thicker film [34]. It is then annealed in argon ambient at 450^0C to relieve the stress induced during deposition and enrich the texture of the material.

Figure 5.6 shows the SEM image of an annealed Pt surface. Figure 5.7 reveals the coarse grain structure of annealed platinum. Figure 5.8 shows an improved intensity in the Pt (111) orientation along with the formation of ternary intermetallic phase (Pt_3Ti). Table 5.2 indicates the intensity of Pt (111) improved by 39 fold on sputtering.

5.2.3 Shift from In-house Sol-Gel Preparation to Company Standard Solution

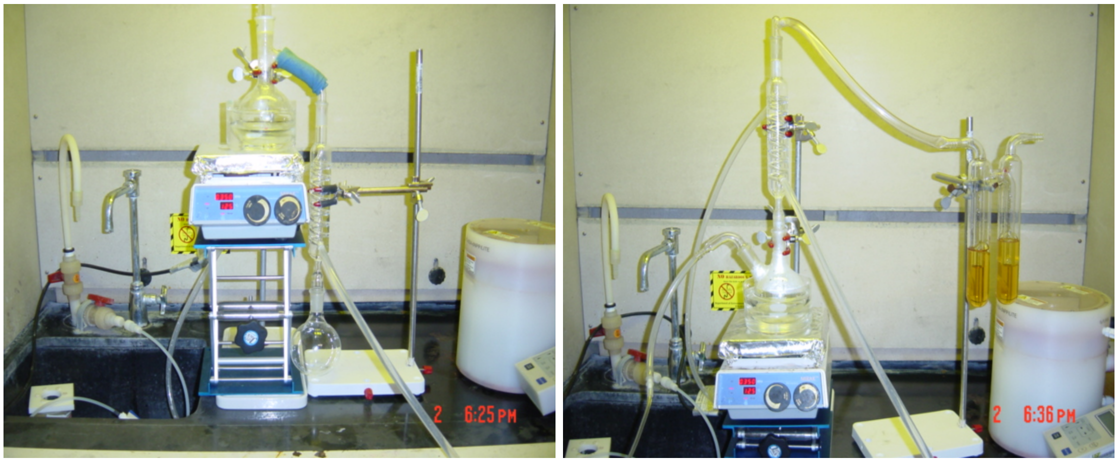

(a) (b)

Figure 5.9 In-house Sol-gel Preparation (a) Distillation Set-Up (b) Reflux Set-Up for In-house Sol-Gel PZT Preparation Using 2MOE as Solvent

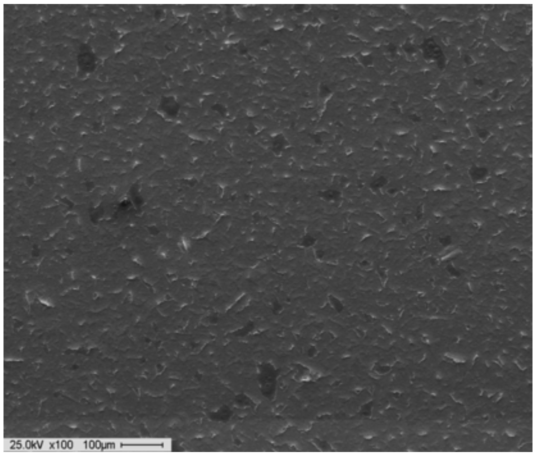

Figure 5.10 SEM (25KV, 0.1K) Image Showing Stress Voiding on PZT Surface on Using 2MOE

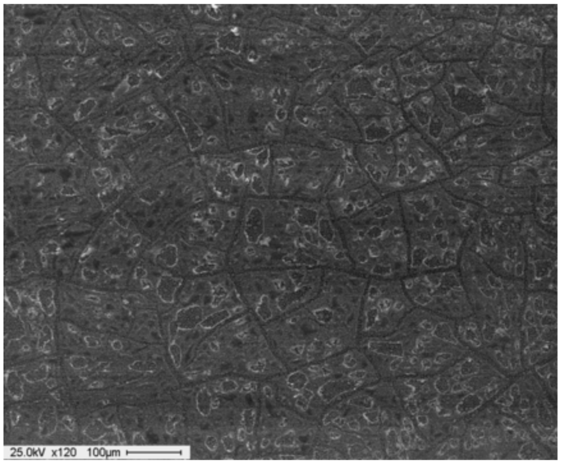

Figure 5.11 SEM (25KV, 0.1K) Image Showing Discontinuous PZT Film Indicating Grain Boundaries

In the early stages of this work, sol-gel PZT [$Pb_{1.15}$ ($Zr_{0.52}Ti_{0.48}$) O_3] was prepared in-house. Figure 5.9 illustrates the distillation and reflux set-up used to concentrate the precursors to form the solution. The recipes with the precursors are described in Appendix A. Two types of solvents namely 2-methoxyethanol (2MOE) and propylene glycol were used to dissolve the precursors. The processing conditions followed for both the solvents were similar. The spin speed was set at 500RPM for 3seconds and then 1500 RPM for a minute. Then the wafer was pyrolized at two different temperatures of 150^0 C and 385^0 C. The procedure was repeated till 3 spins and the annealed in RTA for a minute at 450^0 C. For the next three spins the pyrolysis step remained the same but the crystallization temperature was increased to 600^0 C. The last three spins were densified at 700^0 C. The PZT wafers prepared using 2MOE showed void formation. In the case of propylene glycol, the PZT films were discontinuous revealing grain boundaries during the last stage of annealing. Figure 5.10 shows the SEM image of the stress induced voids in the film. Figure 5.11 represents the SEM image of discontinuous PZT layer. Table 5.3 compares the stoichiometries of final PZT with ideal values. Figure 5.12 depicts the SEM image of the cross-section indicating minor void formation with a columnar grain structure of PZT. Excess lead content in the former and the oxygen content in the latter are attributed to the absurd surface morphology.

Table 5.3 Ideal Vs Measured Stoichiometry

Element	Ideal Stoichiometry (%)	Measured Stoichiometry-2MOE (%)	Measured Stoichiometry-Propylene glycol (%)
Pb	22.33	33.91	11.56
Ti	9.32	13.05	16.14
Zr	10.09	9.52	4.99
O	58.25	43.51	67.31

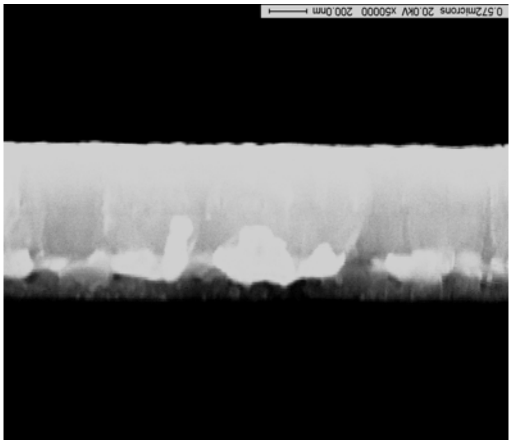

Figure 5.12 Cross Sectional SEM (25KV, 50K) Image of 0.6μm PZT Showing Micro Void Formation

Further optimization of the sol-gel recipe was abandoned due to the lack of precise control over the chemical processes. Currently, the sol-gel PZT (52/48) solution used is procured from Mitsubishi Corp^{TM}. The spin speed is changed to 2100 RPM to suit the viscosity of the solution and the pyrolysis temperature is reduced to 365^0 C. In-order to achieve a thick layer of PZT (1μm), the spin cycle is increased. Figure 5.13 shows the SEM image of the surface after 16 spins.

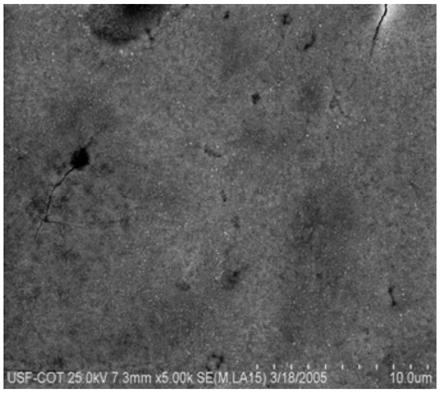

Figure 5.13 SEM (25KV, 5K) Image of the PZT Surface after 16 Spins

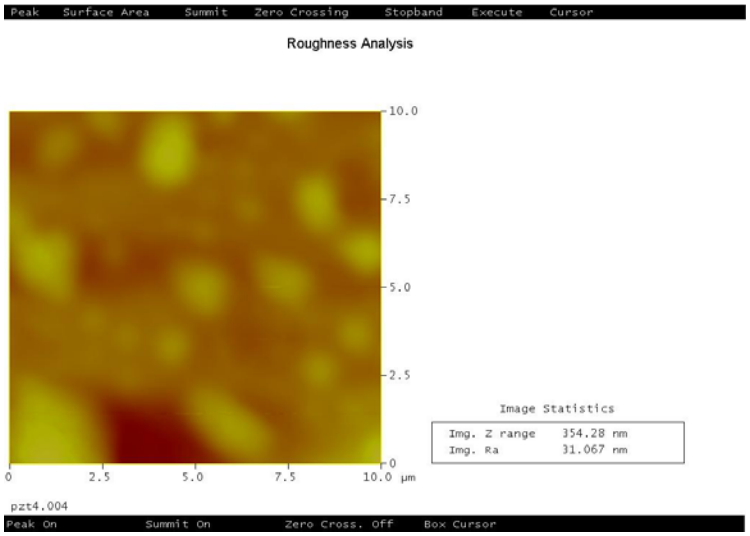

Image Statistics

Img. Z range 354.28 nm
Img. Ra 31.067 nm

Figure 5.14 Average PZT Roughness of 31nm after 16 Spins through AFM

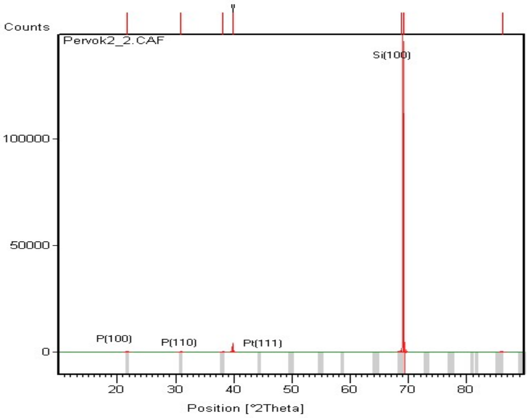

Figure 5.15 XRD Plot Indicating the Absence of Pyrochlore Stage and (111) Texture of PZT under Standard Processing Conditions

The occurrence of crack is minimized. Figure 5.14 indicates the grain size to be 31nm through atomic force microscopy. Figure 5.15 confirms the absence of defective phase at 2thetha value of 28-30^0. The XRD scan is used to calculate the intensity factor (I_{111}) given by the formula:

$$I_{111}=C_{111}/\ (C_{111}+C_{200}+C_{110})\ldots\ (1),$$

Where,

C_{111} = Intensity count in 111 direction

C_{200} = Intensity count in 200 direction

C_{110} = Intensity count in 110 direction

The intensity factor is found to be 39.59 % in favor of perovskite (111) orientation.

5.2.4 Formation of Top Electrode

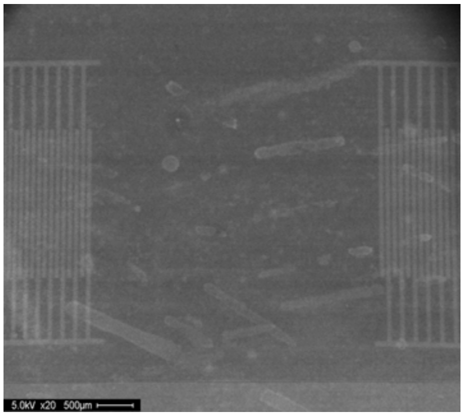

Figure 5.16 SEM (25KV, 0.04K) Image Showing Au IDTs

After depositing the PZT layer, Cr/Au of thickness 200/3000 Å is deposited using a mini thermal evaporator at a working pressure of 10µTorr.The IDT mask having the comb structures is used to define the top electrode. Shipley 1813 positive resist is used in combination with the EVG mask aligner. The process recipe is given in detail in the appendix B. The unwanted Cr/Au is etched back using the gold and chrome etchant for 108secs and 10secs respectively. Finally the resist is stripped using acetone and methanol. Figure 5.16 shows the SEM micrograph of the transmitting and receiving IDTs.

5.2.5 PZT Etching, Poling and P-E Curve

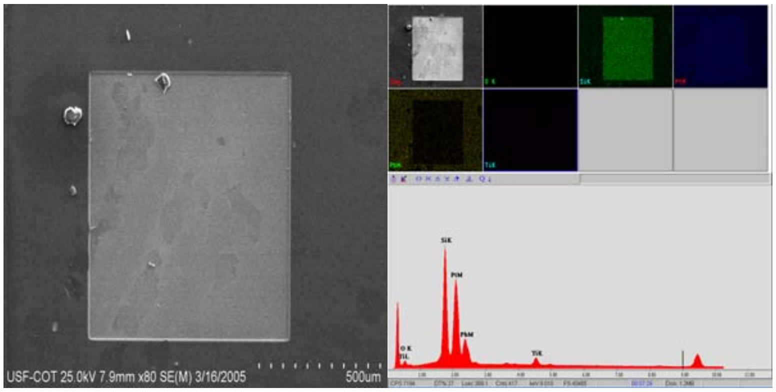

Figure 5.17 SEM (25KV, 80) Micrograph of an Etched PZT Window and EDS Spectrum of Various Possible Elements for Verification

Figure 5.18 Poling Set-Up Using DC Probes

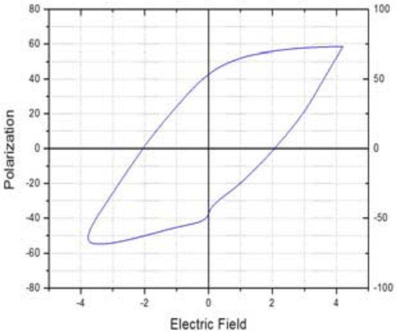

Figure 5.19 Typical Hysteresis Curve (Scale X-axis 1unit =16KV/cm, Y-axis 1unit=12.5μC/cm^2)

In order to ensure the integrity between the IDT pairs, a continuity check is performed. A small portion of PZT is etched to expose the platinum ground plane. Initially PZT was etched in 1:2:4:4 buffered HF (BHF): HCl: NH_4Cl:H_2O [35] for 2 mins. A white layer appears due to the formation of transition fluorides which is further etched in $2HNO_3$:$1H_2O$ for 10-15 seconds. However, a slight increase in the etch time removes the platinum layer. Hence a suitable etchant has to be used which will selectively etch the PZT completely. Finally, 1μm PZT is successfully etched in buffered oxide etch (BOE-10:1) at a etch rate of 0.142μm/min.The etching process is verified using Energy Dispersive Spectroscopy (EDS) maps. Figure 5.17 represents the EDS spectra with a SEM micrograph to confirm the end of a clean etch process. The central square window shown in Figure 5.17 is the PZT etched region exposing platinum. The individual spectra of elements reveal the complete etching process of PZT.

The sample is poled to align the ferroelectric domains. A DC bias of 15V is applied between the top and bottom electrode for 20 mins using dc probes. Figure 5.18 schematically illustrates the poling set-up.The P-E curve is plotted using RT66A. The input parameters to the ferroelectric tester are: 1) area of the capacitor and the dielectric thickness. Both the variables have to be fed accurately to have the precise ferroelectric properties. It is found that for 1 μm thick PZT roughly 14-15 spins are required as supposed to 12. Figure 5.19 represents the hysteresis curve for the PZT.

The recorded remnant polarization and coercive field values were found to be 56$\mu C/cm^2$ and 32 KV/cm respectively. These values compare favorably with published values [36] of 33 $\mu C/cm^2$ for films in the same order of thickness.

5.2.6 Membrane Definition

The membrane is defined through the oxide and nitride layer. The membrane mask is used to pattern the diaphragm region. A thicker photoresist is employed to withstand the oxide and nitride etches. The negative photoresist NR3000PY is double spun to achieve a thickness of 4.5 μm. It is patterned and exposed in the EVG mask aligner. The specifications are given in appendix B. The CVD oxide is etched in BOE and the nitride layer is removed through reactive ion etching.

5.2.7 Change in Etching Set-up from Conventional Method to Jig Assembly

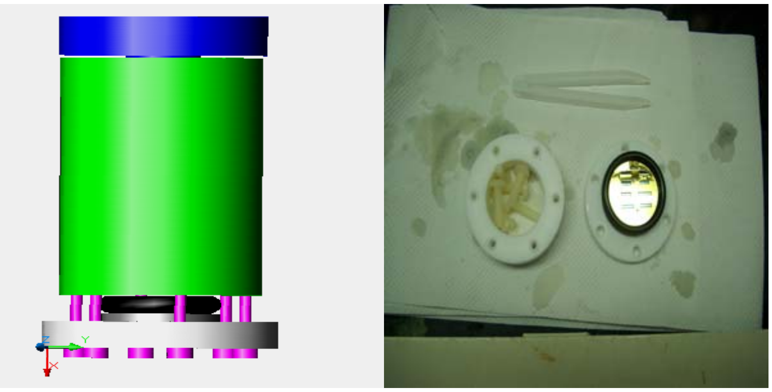

Figure 5.20 Modified Jig Set-up For Etching Silicon

Silicon etchant is selected based on its selectivity toward gold and PZT. The only etchant that offers this property is Ethylene-Di-Amine Pyracatechol (EDP). The preparation and procedure are specially mentioned in the appendix C. However when the wafer with Au/PZT was subjected to EDP etching at 110^{0}C, the silicon was never attacked. After 2 hrs the wafer remained unaffected, while the test wafer with gold on it was etched under similar conditions. Hence it was deduced that there is either an intermediate compound formation between PZT and EDP which prevents the solution from etching silicon or the presence of PZT was passivating the wafer. To validate this hypothesis a dummy patterned silicon wafer is put in the same bath as that of the PZT wafer. The dummy wafer got etched while the PZT wafer remained unchanged.

A jig set up is used to cover the PZT layer and expose the silicon region to the etchant.Figure 5.20 shows the schematic of a modified jig set-up. Normal etch rate of EDP at 110^{0}C is 85 μm/hr. When a jig set-up is used, it drastically reduced to 65μm/hr. A dummy nitride wafer is placed along with the device wafer in the jig for mechanical support. After nearly 4 hrs of etching, 2μm ultra–thin silicon nitride membranes are formed.

Figure 5.21 represents the SEM micrograph of the 2µm silicon nitride membrane. The average roughness of the membrane is found to be 0.3nm.

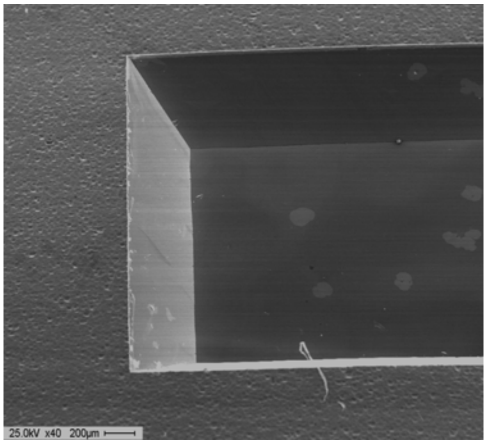

Figure 5.21 SEM (25KV, 0.04K) Image of 2µm Silicon Nitride Membrane

Figure 5.22 Front and Rear View of the Final Device

The final etched device is immersed in isopropanol to get rid of traces of EDP. Figure 5.22 shows the front and rear view of the final device.

Chapter 6

Results and Conclusion

This chapter focuses on the analysis of the results and the derived conclusions from optimized sol-gel processing conditions. A brief note on future work is presented.

6.1 Process Optimizations

The optimization steps discussed in previous chapters are listed as follows:

1. Enhanced Pt(111)-Modified annealing conditions for the bottom electrode
2. Uniform and Homogenous PZT film-Alterations in the spin speed and time
3. Minimal Lead Loss - Change in pyrolysis set-up
4. Excellent Morphology with crack alleviation-Revised annealing procedure

6.1.1 Enhanced Pt (111)-Modified Annealing Conditions for the Bottom Electrode

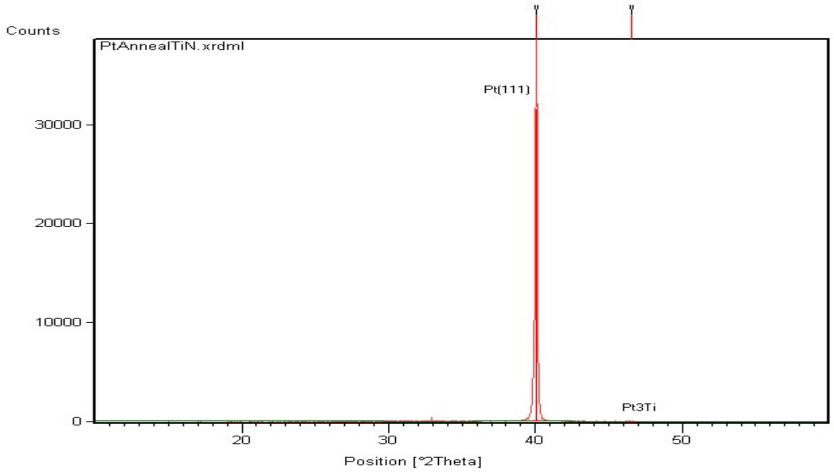

Figure 6.1 XRD Spectra Obtained After Optimized Annealing Conditions for the Bottom Electrode

Table 6.1 Comparison of Pt Intensity in Standard Vs Optimized Processing Conditions

Condition	Pt(111) Intensity [cts]	$Pt_3Ti(111)$ Intensity [cts]
Standard	5460.08	132.72
Optimized	39000	256.75

The bottom electrode Ti/TiN/Pt has profound influence on the texture of PZT film. Three critical properties concerned with PZT crystal growth are amount of impurity diffusion, lattice mismatch and stress due to difference in thermal coefficient of expansion. The impurity diffusion is prevented by using TiN as a barrier layer. The lattice mismatch is found to be 4% between annealed Pt (111) and PZT (111) indicating superior epitaxial conditions for PZT nucleation. Thermally induced stress variation is minimized by annealing platinum in steps of 450^0C, 600^0C and 700^0C each for a minute long in Argon ambient. By performing a sputter deposition of platinum, the intensity that is required for optimized condition is obtained. The Platinum surface is annealed at a temperature closer to the crystallization temperature of PZT avoiding peeling issues. Additionally, the formation of a ternary intermetallic compound Pt_3Ti serves as better nucleation sites for preferred growth of (111) PZT during crystallization. Figure 6.1 shows the XRD spectrum after bottom electrode annealing in optimized conditions. Table 6.1 compares the XRD spectra obtained from industry standard processing with optimized conditions. A reduction in the interfacial energy assures the hetero-epitaxial nucleation.

6.1.2 Uniform and Homogenous PZT film-Alterations in the Spin Speed and Time

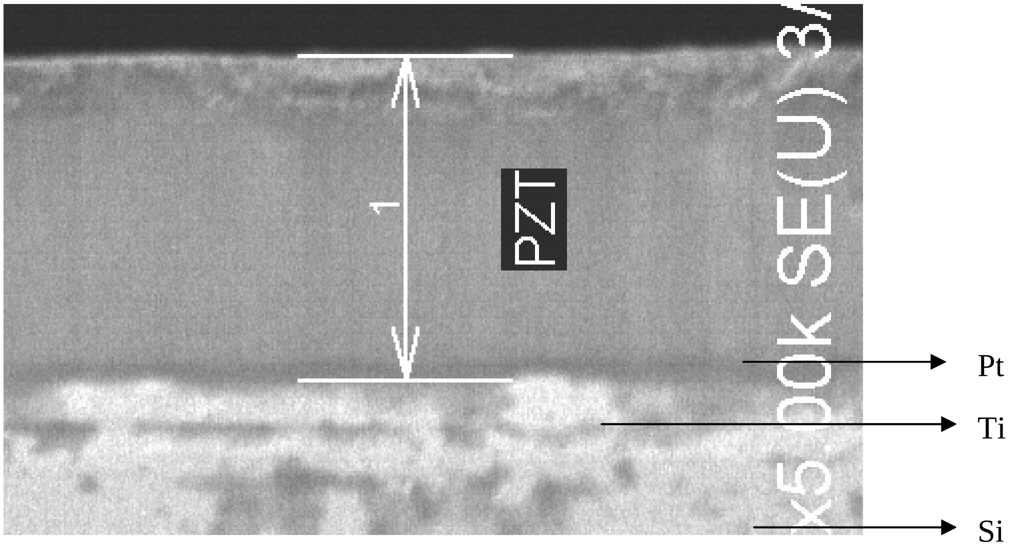

Figure 6.2 SEM (1KV, 5K) Image Showing the Cross Section of a 1µm PZT

The spin speed is set at 500 RPM for 5 seconds and then 2100 RPM for a minute. The number of cycles, which includes spinning and pyrolysis, is increased from 3 to 4 before an annealing step. The number of spins is increased to 15 to achieve 1µm thick PZT for better actuation. The alterations in the spin parameters guaranteed homogenous coating with uniform surface profile. Figure 6.2 shows a SEM micrograph of the cross section of a 1µm thick PZT.

6.1.3 Minimal Lead Loss-Change in Pyrolysis Set-up

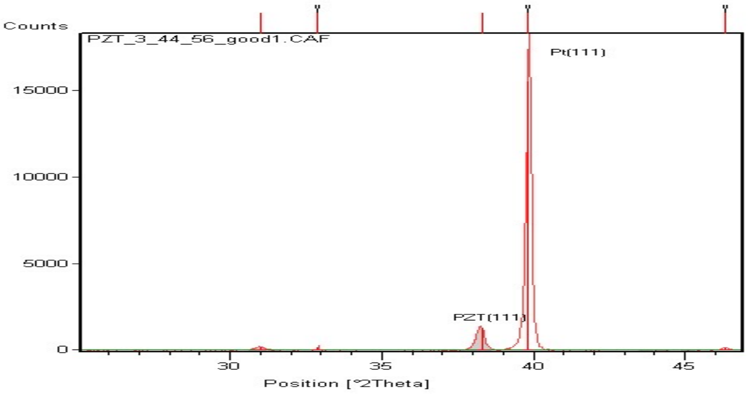

Figure 6.3 XRD Spectra After Multi-Zone Pyrolysis (MZP)

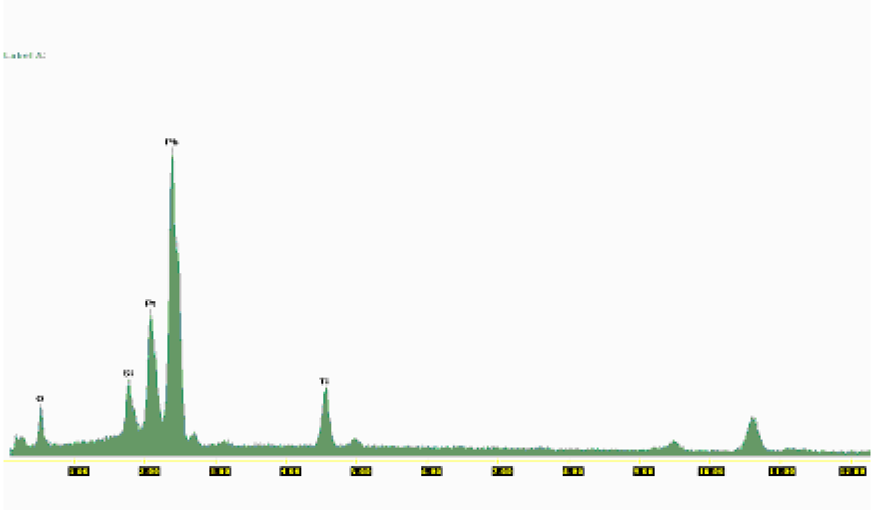

Figure 6.4 EDX Analysis of Sample Prepared Using MZP

Table 6.2 Comparison of Initial Vs Final Composition of Individual PZT Elements

Element	Initial Composition(Atomic Percentage)	Final Composition(Atomic Percentage)
Pb	22.33	20.50
Zr	10.09	10.56
Ti	9.32	9.83
O	58.25	59.11

The pyrolysis temperature dictates the piezoelectric properties and texture of sol-gel PZT. The amount of lead evaporated is a function of pyrolysis temperature and time. A novel approach referred to as “Multi-Zone Pyrolysis” is adopted to minimize lead evaporation yet remove the organic fraction completely. After spinning a layer, the wafer is positioned horizontally with the help of tweezers at a considerable clearance from the hotplate at 345^0 C. The wafer is slowly brought down towards the hot plate stopping at equi-distant zones with varying heat distribution. This can be thought in similar lines of a fractional distillation tower where each volatile compound vaporizes at particular heat zone. The wafer is finally placed in the hot plate for 2 minutes while transversing through different heat zones.

This resulted is an eight fold improvement in the intensity of PZT (111) compared to standard processing conditions. The intensity factor of PZT (111) orientation increased to

93% from a low of 33%. Figure 6.3 shows the XRD spectra illustrating the enhancement in the texture of PZT (111) after annealing. The resulting structure has a $Pb(Ti_{0.44}Zr_{0.56})O_3$ stoichiometry. Figure 6.4 confirms the final composition of the individual components indicating a minimal lead loss of 8%. Table 6.1 compares the initial and final composition of the individual elements after a MZP taking into consideration the back ground signal of titanium from the bottom electrode. The sample is poled with a DC bias of 15V for 15mins. Figure 6.5 represents the P-E curve plotted using the ferroelectric tester (RT66A). The remnant polarization and coercive field are found to be 95.7µC/cm^2 and 56.7 KV/cm respectively nowhere reported in literature.

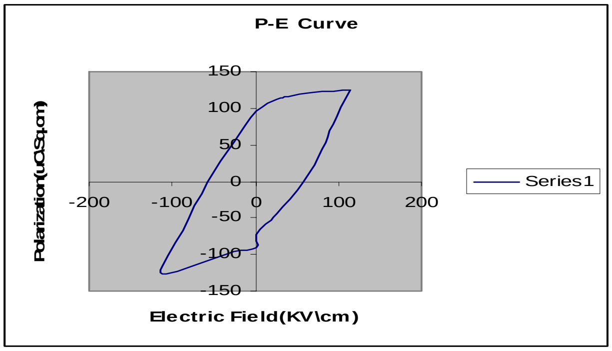

Figure 6.5 Optimized P-E Curve

6.1.4 Revised Annealing Procedure

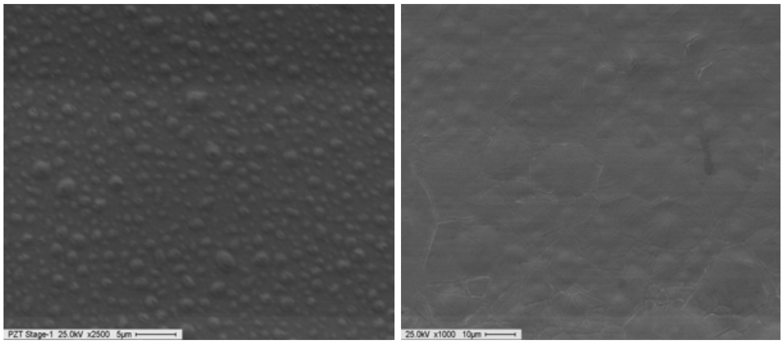

(a) (b)

Figure 6.6 SEM Images of the Morphology of PZT After Annealing (a) After 4 Spins (25KV, 2.5K) (b) After 8 Spins (25KV, 1K) (c) After 12 Spins (25KV, 1K) (d) Zoomed in Image of the Crack (25KV, 7K)

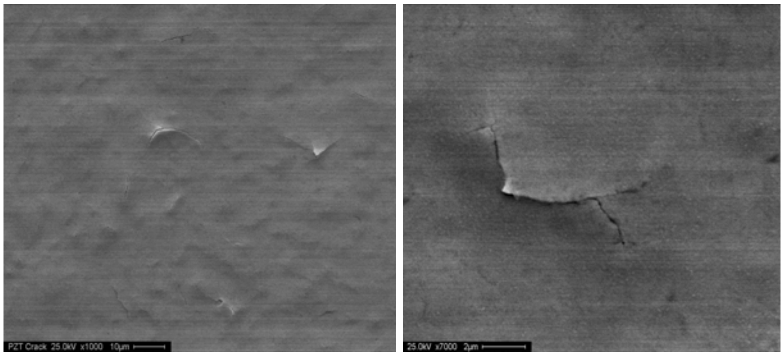

(c) **(d)**

(Continued)

After every four spins and a pyrolysis step, the wafer is annealed for crystallization. The annealing temperature and time are programmed in such a manner that it kinetically delimits the growth of the intermediate defective phase. The annealing temperatures are chosen to be 450^0C, 600^0C and 750^0C with 60 seconds transition at each stage. The flow rate of the oxygen ambient is fixed to be 40SCCM after several experimental trials. In each step of annealing cycle, the PZT is driven towards the morphotropic phase boundary stabilizing the perovskite structure (111). The morphology is improved alleviating the formation of cracks. Figure 6.6 depicts the microstructural evolution of PZT. The morphology obtained is characteristic of a Zr-rich phase.

6.2 Conclusions

This work presents an alternate processing methodology for improving the morphology and texture of PZT (111) film. All the sol-gel processing variables are inspected to identify the tuning parameter. The bottom electrode is found to have profound effect on the texture of PZT. Subsequent thermal stages are executed with a close watch on the induced stress. PZT films with superior ferroelectric properties are reported. Alterations in the process flow lead to improved repeatability in device fabrication. Through a careful process development and optimization of PZT thin film, a highly sensitive flexural plate wave device is fabricated.

6.3 Future Work

The optimized conditions for sol-gel PZT would be utilized to fabricate a sensitive hydrogen sensor. As a measure of completeness, PZT will also be deposited by sputtering and pulsed laser ablation. The piezoelectric properties will be compared to sol-gel method developed. The variation of piezoelectric properties with changing substrates would be studied. Diamond will be one of the potential candidates due to its high acoustic velocity.

References

[1] D.S.Ballatine, Jr et al., "Acoustic Wave Sensors: Theory, Design and Physico Chemical Application", Academic Press,1997.

[2] www.memsnet.org

[3] Amy W. Wang, Radwan Kiwan, Richard M. White and Roberto L. Ceriani, "A silicon-based ultrasonic immunoassay for detection of breast cancer antigens", Sensors and Actuators B: Chemical, Volume 49, Issues 1-2, 25 June 1998, PP. 13-21.

[4] Nam-Trung Nguyen, Audra H. Meng, Justin Black and Richard M.White, "Integrated flow sensor for in situ measurement and control of acoustic streaming in flexural plate wave micropumps" , Sensors and Actuators A: Physical, Volume 79, Issue 2, 1 February 2000, P. 115-121.

[5] Brian Cunningham, Marc Weinberg, Jane Pepper, Chris Clapp, Rob Bousquet, Brenda Hugh, Richard Kant, Chris Daly and Eric Hauser, "Design, fabrication and vapor characterization of a microfabricated flexural plate resonator sensor and application to integrated sensor array", Sensors and Actuators B: Chemical, Volume 73, Issues 2-3, 10 March 2001, P. 112-123.

[6] www.physikinstrumente.com

[7] S.Akella, "Development of Lead Zirconate Titanate Based Flexural Plate Wave Actuator", Master's Thesis, USF, Tampa, 2005.

[8] www.utdallas.edu/~jblee/EE7v82/ UTD%20MEMS%2027%20Piezoelectricity.pdf

[9] Piezoelectric Ceramics: Principles and Applications, APC International Ltd, 2003.

[10] Thompson.M and Stone C.D, “Surface-launched acoustic wave sensors: chemical sensing and thin-film characterization”, Wiley, 1997.

[11] www.rclsgi.eng.ohio-state.edu/courses/me570/InstsurveyII04.ppt

[12] Q. Q. Zhang, S. J. Gross, S.Tadigadapa, T. N. Jackson, F. T. Djuth and S. Trolier McKinstry, “Lead Zirconate Titanate films for d_{33} mode cantilever actuators”, Sensors and Actuators A: Physical, Volume 105, Issue 1, 15 June 2003, P. 91-97.

[13] Wenzel, S.W.; White, R.M., “Flexural plate-wave sensor: chemical vapor sensing and electrostrictive excitation”, Ultrasonics Symposium, Volume 1, 1989, P. 595 – 598.

[14] Weinberg, M.S.; Dube, C.E.; Petrovich, A.; Zapata, A.M., “Fluid damping in resonant flexural plate wave device”, Journal of Microelectromechanical Systems, Volume 9, Issue 3 , Sept. 2000, P. 370 – 379.

[15] Ph. Luginbuhl, S. D. Collins, G. -A. Racine, M. -A. Grétillat, N. F. De Rooij, K. G. Brooks and N. Setter, “Ultrasonic flexural Lamb-wave actuators based on PZT thin film”, Sensors and Actuators A: Physical, Volume 64, Issue 1, 1 January 1998, PP. 41-49.

[16] Clifford Frederick Knollenberg, “Sputter Deposition of Piezoelectric Lead Zirconate Titanate Thin Films for Use in MEMS Sensors and Actuators”,Master’s Thesis, UC-Berkeley.

[17] http://aml.seas.ucla.edu

[18] Rajasekhar Popuri, “The Development of Lead Zirconate Titanate Thin Films for Piezoelectric Microsensors and Microactuators”, Master’s Thesis, USF, Tampa,2003.

[19] Masaru Shimizu, Hironori Fujisawa, Hirohiko Niu and Koichiro Honda, “Growth of ferroelectric $PbZr_xTi_{1-x}O_3$ thin films by metalorganic chemical vapor deposition”, Journal of Crystal Growth, Volumes 237-239, Part 1, April 2002,P. 448-454.

[20] Kazuyoshi Tsuchiya, Toshiaki Kitagawa and Eiji Nakamachi, “Development of RF magnetron sputtering method to fabricate PZT thin film actuator”, Precision Engineering, Volume 27, Issue 3, July 2003, P. 258-264.

[21] R. Dat, O. Auciello and A. I. Kingon, “Surface roughness of $PbZr_xTi_{1-x}O_3$ thin films produced by pulsed laser ablation-deposition”, Thin Solid Films, Volume 283, Issues 1-2, 1 September 1996, P. 45-48.

[22] L. Meidong, L. Chunru, W. Peiying, R. Yunhua, Z. Yike and L. Churong, “Preparation of PZT ferroelectric thin films by sol-gel processing and their properties”, Sensors and Actuators A: Physical, Volume 49, Issue 3, July 1995, P. 191-194.

23] H. N. Al-Shareef, K. R. Bellur, O. Auciello and A. I. Kingon,“Phase evolution and annealing effects on the electrical properties of $Pb(Zr_{0.53}Ti_{0.47})O_3$ thin films with RuO_2 electrodes”, Thin Solid Films, Volume 256, Issues 1-2, 1 February 1995, P. 73-79.

[24] D. Van Genechten, G. Vanhoyland, J. D'Haen, J. Johnson, D. J. Wouters, M. K. Van Bael, H. Van den Rul, J. Mullens and L. C. Van Poucke, “Phase evolution of sol–gel prepared $Pb (Zr_{0.3}Ti_{0.7})O_3$ thin films deposited on $IrO_2/TiO_2/SiO_2/Si$ electrodes”, Thin Solid Films, Volume 467, Issues 1-2, 22 November 2004, P. 104-111.

[25] Lulu Zhang, Masaaki Ichiki and Ryutaro Maeda, “Residual stresses in Pt bottom electrodes for sol-gel derived lead zirconate titanate thin films”, Journal of the European Ceramic Society, Volume 24, Issue 6, 2004, PP. 1673-1676.

[26] S. -H. Kim, Y. -J. Oh and C. -E. Kim, “Influence of Al_2O_3 diffusion barrier and $PbTiO_3$ seed layer on microstructural and ferroelectric characteristics of PZT thin films by sol-gel spin coating method”, Thin Solid Films, Volume 305, Issues 1-2, August 1997, P. 321-326.

[27] Wen Gong, Jing-Feng Li, Xiangcheng Chu and Longtu Li, “Effect of pyrolysis temperature on preferential orientation and electrical properties of sol-gel derived lead zirconate titanate films”, Journal of the European Ceramic Society, Volume 24, Issues 10-11, September 2004, P. 2977-2982.

[28] Dwight Viehland, Jie-Fang Li, Xunhu Dai and Z. Xu, “Structural and property studies of high Zr-content lead zirconate titanate”, Journal of Physics and Chemistry of Solids, Volume 57, Issue 10, October 1996, P. 1545-1554.

[29] www.mmea.com/pdf/PZT_Solgel.pdf

[30] Jing Yang and Luo Jianbin, “Processing and thickness effects on the microstructure and electrical properties of sol–gel deposited Pb (Zr, Ti)O_3 films”, Sensors and Actuators A: Physical.

[31] J. Perez, P. M. Vilarinho and A. L. Kholkin, “High-quality $PbZr_{0.52}Ti_{0.48}O_3$ films prepared by modified sol–gel route at low temperature”, Thin Solid Films, Volume 449, Issues 1-2, 2 February 2004, P. 20-24.

[32] Chang Jung Kim, Dae Sung Yoon, Zhomg-Tao Jiang, Kwangsoo No,“Investigation of the drying temperature dependence of the orientation in sol–gel processed PZT thin films”, Journal Of Materials Science,32,1997, P. 1213-1219.

[33] Ji-Eun Lim, Dong-Yeon Park, Jae Kyeong Jeong, Gregor Darlinski, Hyeong Joon Kim,and Cheol Seong Hwang, “Dependence of ferroelectric performance of sol–gel-derived Pb.Zr,Ti.O3 thin films on bottom-Pt-electrode thickness”, Applied Physics Letter, Vol81, No.17 , P. 3224-3226.

[34] Kelu Zheng; Jian Lu; Jiaru Chu; “Study on wet-etching of PZT thin film”, Microprocesses and Nanotechnology Conference, Volume 29-31, 2003, P. 248 – 249.

[35] X. G. Tang, L. L. Jiang and A. L. Ding,” The effect of thickness on the dielectric properties of highly (111) oriented $Pb(Zr_{0.53}Ti_{0.47})O_3$ thin films prepared by a simple sol–gel route”, Microelectronic Engineering, Volume 65, Issue 4, May 2003, P. 387-393.

Appendices

Appendix A: Preparation of (52/48) Sol-Gel PZT Solution Using 2MOE

To prepare a 100mL, 0.5 molarity batch of 52/48 PZT solution with 15% excess Pb ($Pb_{1.15}(Zr_{0.52}Ti_{0.48})O_3$), the amount of chemicals to be added are calculated in this manner.

Pb: (0.5mol/L)(0.1L)(379.33g/mol)(1.15) = 21.812g

Zr: (0.5mol/L)(0.1L)(327.58g/mol)(0.52)$(0.7)^{-1}$ = 12.167g

Ti: (0.5mol/L)(0.1L)(284.26g/mol)(0.48) = 6.822g

Process Steps

1. Obtain the distillation setup, reflux setup, glove bag, two neck flask, stirrers, scale, scoopers, droppers, and required chemicals for PZT synthesis.
2. Place the beaker with oil on the hotplate and insert the temperature probe through the tinfoil. Make sure that the probe is immersed but does not touch the sides or the bottom of the beaker. Set the probe temperature to 115ºC. Set the stir bar on hot plate to 350 rpm.
3. Put 250ml round bottom flask (with stirrer in it) in the glove bag. Purge the glove bag 3 times. Make sure that the pressure in the glove bag is higher than room pressure.
4. Bring flask and stirrer into glove bag. Level scale, and zero with flask on it. Add 21.812g of lead acetate trihydrate to flask. Add propylene glycol until flask is approximately half full.
5. Check oil bath temperature (should be ~115ºC), and set up distillation components as shown below.

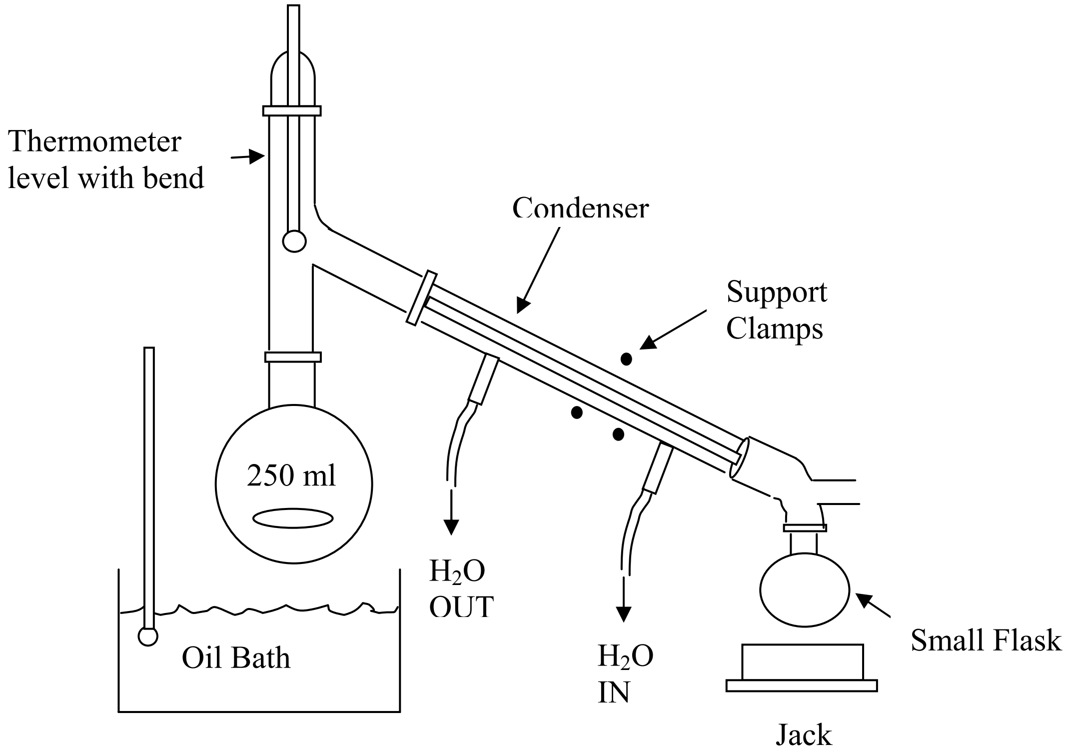

Figure A.1 Distillation Set-up for PZT Synthesis

6. Raise oil bath around flask with lead/solvent (oil should be slightly above level of solvent). Make sure stirrer in the flask spins. Check to make sure joints are tight.
7. Distill for 2 hours.
8. After two hours of distillation, lower oil bath and allow flask to cool for 20 min.
9. Put the round bottom flask and a two neck flask into glove bag and purge. Once in the glove bag, transfer solution and stirrer to two neck round bottom flask. Rinse original flask with a small amount of solvent, and pour into two neck flask. Put the two neck flask on scale, zero scale, and add 12.167g of zirconium tetra n-butoxide. Zero scale

again, and add 6.82g of titanium tetra-iso-propoxide (use separate droppers for each). Dispose of droppers in waste jar.

10. Take two neck flasks out of glove bag, and set up reflux equipment as shown below.

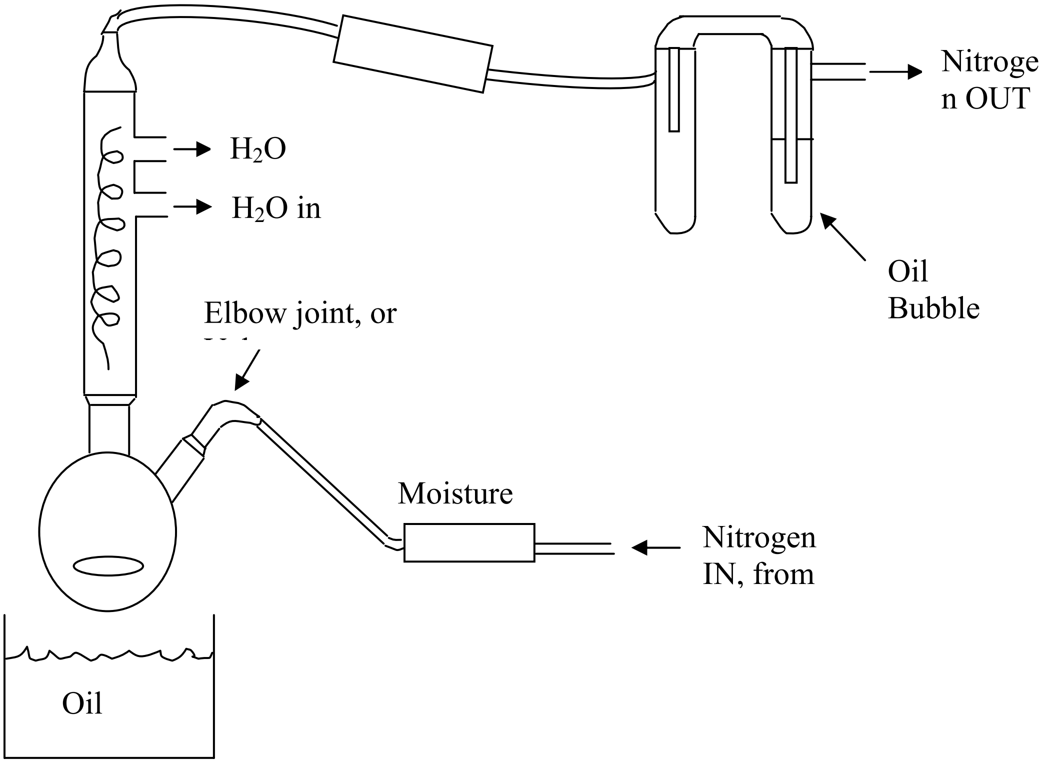

Figure A.2 Reflux Set-up for PZT Synthesis

11. Barely crack open the nitrogen tank.
12. Raise oil bath and reflux for 3 hours. Do not allow oil bath to exceed 110ºC.
13. After 3 hours, lower oil bath and allow it to cool for 20 minutes.

Appendix A (Continued)

14. Set up distillation equipment again (wash it after the first distillation and oven dry). Put the two neck flasks and regular round bottom flask in the glove bag. Transfer solution back to original round bottom flask. Rinse two-neck flask with a small amount of solvent and add to rest of solution.
15. Perform distillation until there is less than 100ml in the flask (shoot for about 75ml). This usually takes between 1.5 – 2 hours.
16. After distillation is complete, put flask in the glove bag along with a graduated cylinder, and a jar. Measure the final amount of solution. Then add solvent until there is 100 ml of total solution. Put all solution and magnet into the small glass bottle.
17. Label the glass bottle, clean glass ware and allow it to stir overnight (no heat).

Appendix B: Processing Conditions for Resist S1813 and NR 3000PY in EVG Mask Aligner

(a) Processing Conditions for S1813 resist

Spin speed: 2500RPM
Spin Time: 1 minute
Soft Bake: 90^0C, 1 minute
Exposure Time: 9 seconds
Developer: MIF-319
Developing Time: 70 seconds
Hard Bake: 110^0C , 1 minute
Thickness of resist obtained: 1.34 μm
Adhesion Promoter: Hexamethylenedisilizane
Type of Resist: Positive

(b) Processing Conditions for NR 3000PY resist

Spin speed: 3000RPM
Spin Time: 40 seconds
Soft Bake: 155^0C, 1 minute
Exposure Time: 19 seconds
Developer: RD-6
Developing Time: 25 seconds
Hard Bake: 110^0C, 1 minute
Thickness of resist obtained: 3.34 μm
Adhesion Promoter: none
Type of Resist: Negative

Appendix C: EDP Preparation

Table C.1 EDP Mixture Preparation

Materials	Single	Double	Triple
DI water	48 ml	96 ml	144 ml
Catechol	48 g	96 g	144 g
Pyrazine	0.9 g	1.8 g	2.7 g
Ethylenediamene	150 ml	300 ml	450 ml

C.1 EDP Procedure

1. Obtain an EDP beaker, a graduated cylinder labeled “Ethylene Di-amine”, the scale, a large plastic weigh boat, a small plastic weigh boat, and a piece of tinfoil to cover the beaker.
2. Place an EDP waste bottle in the sink. Make sure that the hotplate is covered with two layers of clean tinfoil.
3. Measure the DI water in the graduated cylinder and add it to the beaker.
4. Weigh out the catechol in the large plastic weigh boat: add it to the beaker. Discard the weigh boat in the small EDP trash can. Wipe off the lip and outside of the catechol bottle before returning it to the cabinet.
5. Weigh out the pyrazine in the small plastic weigh boat: add it to the beaker. Discard the weigh boat in the small EDP trash can. Wipe down the outside of the pyrazine bottle before returning it to the cabinet. Wipe down the scale before returning it to the shelf.
6. Place the large graduated cylinder in the sink. Measure out the ethylenediamine and pour it in the beaker. Immediately cover the beaker with tinfoil. Rinse the graduated cylinder with DI water: pour the water from the first two rinses into the

7. EDP waste bottle. Rinse the graduated cylinder three more times before returning it to the shelf. Wipe down the outside of the ethylenediamine bottle before returning it to the cabinet.
8. Place the beaker on the hotplate and insert the temperature probe through the tinfoil. Make sure that the probe is immersed but does not touch the sides or the bottom of the beaker. Set the probe temperature to 110ºC. Do not allow EDP to boil.
9. After the EDP has reached the correct temperature, add your samples. The etch rate at 110ºC is approximately 80µm/hour.
10. Post a notice with your name, date and time, and a phone number where you can be reached on the door of the hood.

C.2 Waste Handling

C.2.1 Solid waste

All solid trash generated during an EDP etch should be deposited in the small EDP trash can. This includes paper towels, weigh boats, plastic scoopers, gloves etc.EDP may not be poured down the drain. EDP must be disposed of in properly labeled hazardous waste bottles. Never tightly cap a bottle containing hot EDP waste or it may explode. Loosely place the cap on the bottle and leave it at the back of the hood until it is sufficiently cool. Then tighten the cap, wipe down the outside of the bottle, and put it in the waste chemical cabinet.